Title
A comparison of oceanic and continental mantle lithosphere

Authors
Fischer, Karen M
Rychert, Catherine A
Dalton, Colleen A
et al.

Publication Date
2020-12-01

DOI
10.1016/j.pepi.2020.106600

Peer reviewed

Physics of the Earth and Planetary Interiors 309 (2020) 106600

Contents lists available at ScienceDirect

Physics of the Earth and Planetary Interiors

journal homepage: www.elsevier.com/locate/pepi

Review

A comparison of oceanic and continental mantle lithosphere

Karen M. Fischer [a,*], Catherine A. Rychert [b], Colleen A. Dalton [a], Meghan S. Miller [c], Caroline Beghein [d], Derek L. Schutt [e]

[a] Department of Earth, Environmental and Planetary Sciences, Brown University, Providence, RI 02912, USA
[b] School of Ocean and Earth Science, National Oceanography Centre Southampton, University of Southampton Waterfront Campus, European Way, Southampton SO14 3ZH, United Kingdom
[c] Research School of Earth Sciences, The Australian National University, Building 142, Mills Road, Canberra, ACT 2601, Australia
[d] Department of Earth, Planetary, and Space Sciences, University of California, Los Angeles, CA 90095, USA
[e] Department of Geosciences, Colorado State University, Fort Collins, CO 80523, USA

A B S T R A C T

Over the last decade, seismological studies have shed new light on the properties of the mantle lithosphere and their physical and chemical origins. This paper synthesizes recent work to draw comparisons between oceanic and continental lithosphere, with a particular focus on isotropic velocity structure and its implications for mantle temperature and partial melt. In the oceans, many observations of scattered and reflected body waves indicate velocity contrasts whose depths follow an age-dependent trend. New modeling of fundamental mode Rayleigh waves from the Pacific ocean indicates that cooling plate models with asymptotic plate thicknesses of 85-95 km provide the best overall fits to phase velocities at periods of 25 s to 250 s. These thermal models are broadly consistent with the depths of scattered and reflected body wave observations, and with oceanic heat flow data. However, the lithosphere-asthenosphere velocity gradients for 85-95 km asymptotic plate thicknesses are too gradual to generate observable Sp phases, both at ages less than 30 Ma and at ages of 80 Ma or more. To jointly explain Rayleigh wave, scattered and reflected body waves and heat flow data, we propose that oceanic lithosphere can be characterized as a thermal boundary layer with an asymptotic thickness of 85-95 km, but that this layer contains other features, such as zones of partial melt from hydrated or carbonated asthenosphere, that enhance the lithosphere-asthenosphere velocity gradient. Beneath young continental lithosphere, surface wave constraints on lithospheric thickness are also compatible with the depths of lithosphere-asthenosphere velocity gradients implied by converted and scattered body waves. However, typical steady-state conductive models consistent with continental heat flow produce thermal and velocity gradients that are too gradual in depth to produce observed converted and scattered body waves. Unless lithospheric isotherms are concentrated in depth by mantle upwelling or convective removal, the presence of an additional factor, such as partial melt at the base of the thermal lithosphere, is needed to sharpen lithosphere-asthenosphere velocity gradients in many young continental regions. Beneath cratons, numerous body wave conversions and reflections are observed within the thick mantle lithosphere, but the velocity layering they imply appears to be laterally discontinuous. The nature of cratonic lithosphere-asthenosphere velocity gradients remains uncertain, with some studies indicating gradual transitions that are consistent with steady-state thermal models, and other studies inferring more vertically localized velocity gradients.

1. Introduction to the lithosphere

Constraints on the boundary layers of the convecting mantle, including the outermost boundary layer that coincides with the lithosphere, are crucial for understanding plate tectonics and mantle dynamics. While the lithosphere is often defined as a mechanically strong layer that overlies weak asthenospheric mantle, the combination of physical and chemical properties that contribute to this rheological transition is uncertain, and multiple definitions of the lithosphere uneasily co-exist in the literature. In classic geodynamic models, the rigid lithosphere corresponds to the conductive portion of the outer thermal boundary layer, while temperatures in the lower viscosity convecting mantle lie close to a mantle adiabat (e.g. Sleep, 2005). Thermal gradients such as these produce a first-order signature in seismic velocities (e.g. Jackson and Faul, 2010). The lithosphere is also described as a compositionally distinct layer that is often explained as a consequence of melt depletion during crust formation (e.g. Hirth and Kohlstedt, 1996; Lee et al., 2011). However, the velocity decrease due to this type of compositional change is subtle (e.g. Schutt and Lesher, 2006; Afonso et al., 2010; Afonso and Schutt, 2012). The effects of partial melt, volatile content, and grain size also influence the viscosity and seismic properties of the rocks at upper mantle depths (e.g. Hirth and Kohlstedt, 1995; Karato and Jung, 1998; Jackson et al., 2006; Takei and Holtzman, 2009; Jackson and Faul, 2010; Karato, 2012; Chantel et al., 2016) adding additional nuance to lithospheric definitions.

Although previous reviews have explored seismological constraints

* Corresponding author.
E-mail address: Karen_Fischer@brown.edu (K.M. Fischer).

https://doi.org/10.1016/j.pepi.2020.106600
Received 2 May 2020; Received in revised form 3 September 2020; Accepted 23 October 2020
Available online 4 November 2020

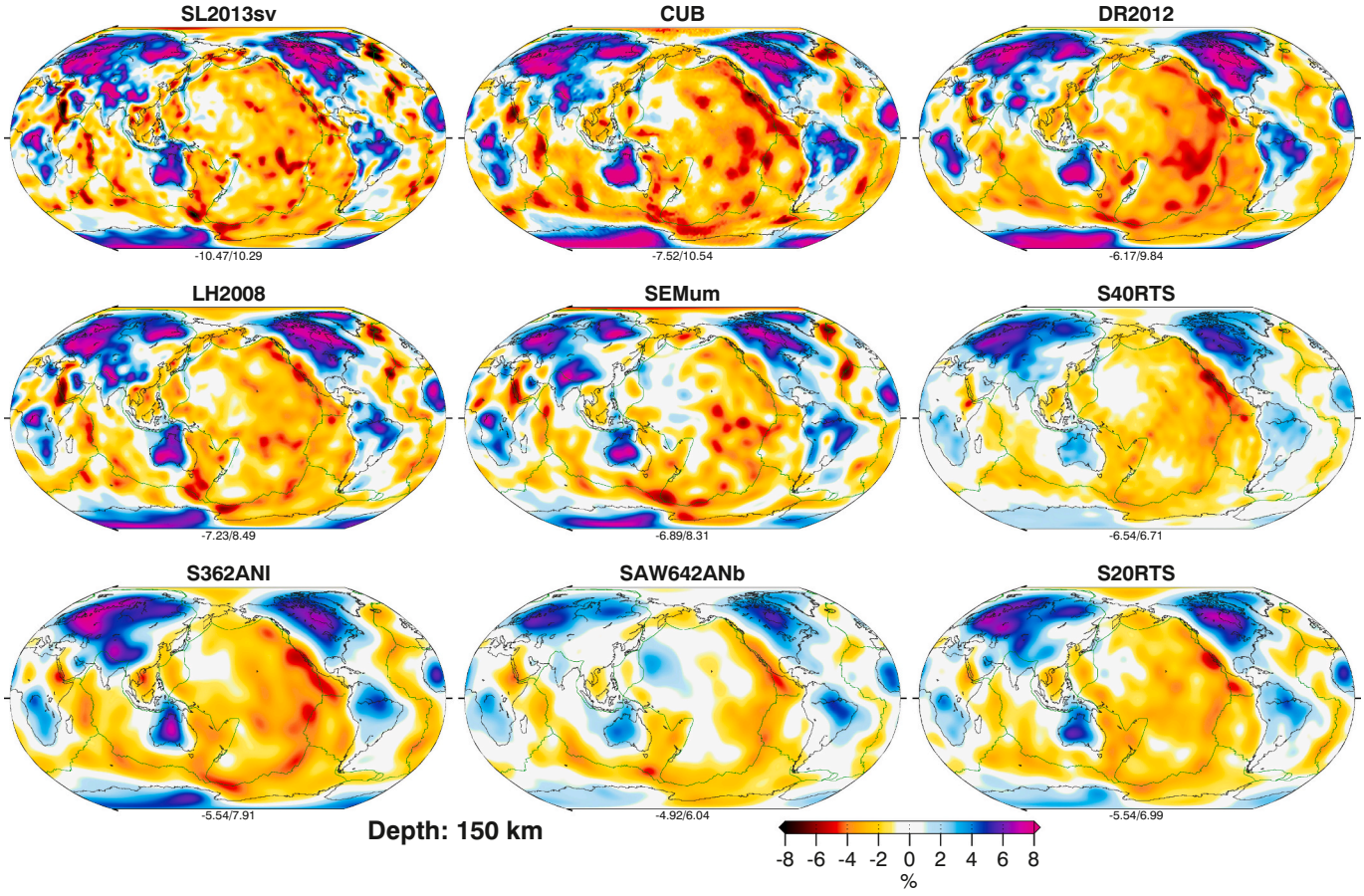

Fig. 1. From Schaeffer and Lebedev (2015). Comparison of velocity anomalies from nine global tomographic models at a depth of 150 km. The models are: SL2013sv (Schaeffer and Lebedev, 2013), DR2012 (Debayle and Ricard, 2012), SEMum (Lekic and Romanowicz, 2011), S40RTS (Ritsema et al., 2011), SAW642ANb (Panning et al., 2010), LH2008 (Lebedev and van der Hilst, 2008), S362ANI (Kustowski et al., 2008), S20RTS (Ritsema et al., 2004), and CUB (Shapiro and Ritzwoller, 2002). Percentages indicate perturbations with respect to the mean absolute shear velocity of the model, and the same color scale is used throughout. Minimum and maximum perturbations are indicated beneath each map. Reprinted by permission from Springer Nature: Global Heterogeneity of the Lithosphere and Underlying Mantle: A Seismological Appraisal Based on Multimode Surface-Wave Dispersion Analysis, Shear-Velocity Tomography, and Tectonic Regionalization, A. J. Schaeffer and S. Lebedev, in *The Earth's Heterogeneous Mantle*. Copyright 2015.

on the lithosphere-asthenosphere boundary (LAB) (e.g. Eaton et al., 2009; Fischer et al., 2010; Rychert et al., 2010; Fischer, 2015; Rychert et al., 2018a), in this study we provide an updated summary of broad-band seismological studies with the goal of comparing the LAB properties of oceans and continents. This comparison raises the question of whether surface waves, which provide constraints on absolute shear velocity structure, and scattered and reflected body wave phases, which are sensitive to velocity interfaces, are consistent with the same lithospheric thickness in oceanic settings. We address this question by testing the range of lithospheric thicknesses that best match surface and body wave observations across the Pacific ocean.

2. Oceanic lithosphere

A first order feature of the lithosphere beneath the oceans is that it is thinner than the lithosphere beneath stable continental interiors. This result is demonstrated by global seismic velocity models. In these models, high seismic velocities associated with the lithosphere of continental interiors persist to depths of 150 km or more, while sub-oceanic velocities are lower in this depth range (Fig. 1). The oceanic lithosphere also has a relatively short and simple history, in comparison to the continents, and its evolution can be described to first order using simple thermal models. Oceanic lithosphere is formed at mid-ocean ridges, where two plates diverge and the underlying mantle rises to replace it. The lithosphere then cools and thickens as it ages and moves away from the ridge. Finally, it descends back into the mantle when it reaches another, generally more buoyant tectonic plate at a subduction zone. The half-space cooling model (Parsons and Sclater, 1977) is the first-order model used to describe the thermal evolution of a column of hot mantle as it moves laterally away from the spreading center. In this model the thickness of the conductive layer, seafloor depth and inverse heat flow are predicted to increase in proportion to the square root of the age of the oceanic lithosphere. This relationship is supported by observational evidence including decreasing heat flow and increasing ocean depth with plate age (Turcotte and Oxburgh, 1967; Hasterok, 2013a).

Although oceanic lithosphere represents a relatively simple version of a tectonic plate, and a thermal model satisfies most observations to first order, some other observations suggest additional complexity. The classic example is that the oldest lithosphere, greater than approximately 70 Myr, does not continue to subside with age as predicted by half-space cooling (Parsons and Sclater, 1977; Watts, 1978; Stein and Stein, 1992). This has been observed in heat flow data, bathymetry, and a few tomographic models (Parsons and Sclater, 1977; Stein and Stein, 1992; Ritzwoller et al., 2004; Ma and Dalton, 2019). An additional heat source is generally thought to cause the divergence from half-space cooling. Empirical models have been developed that employ different thermal boundary conditions at depth to describe the thermal plate structure that satisfies the observed bathymetry and heat flow beneath older seafloor (Parsons and Sclater, 1977; Stein and Stein, 1992; Doin and Fleitout, 1996; Crosby and McKenzie, 2009), a classic example

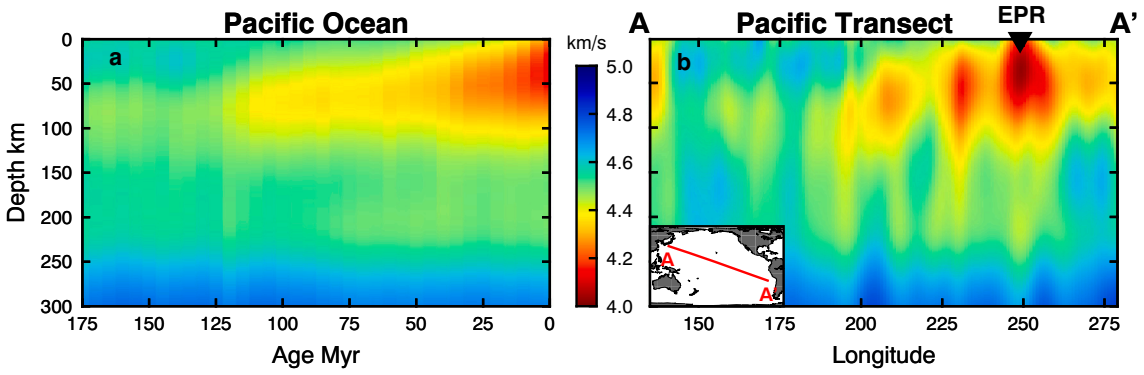

Fig. 2. After Rychert and Harmon (2018). Voigt averaged shear velocities beneath the Pacific from SEMum2 (French et al., 2013). (a) The Pacific averaged by age in 5 Ma bins and (b) a single northwest–southeast transect. Triangle indicates location of the East Pacific Rise (EPR).

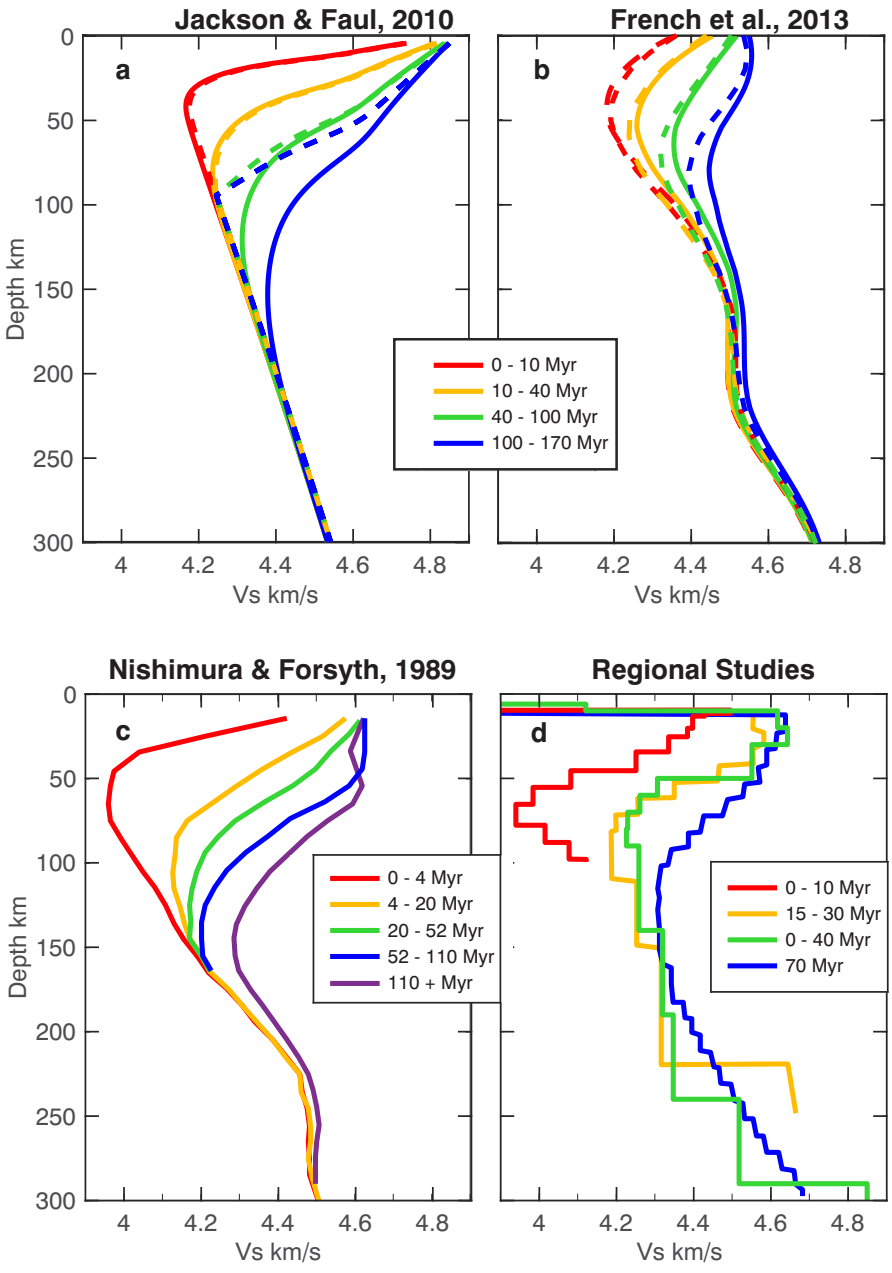

Fig. 3. Depth profiles of shear velocity in the oceanic upper mantle. (a) Predictions using the anelastic parameterization of Jackson and Faul (2010) assuming a grain size of 10 mm applied to thermal profiles calculated with half-space cooling (solid) and the plate model with 95 km plate thickness (dashed). (b) Globally averaged V_{SV} (dashed) and Voigt-averaged isotropic V_S (solid) profiles across the Pacific from SEMum2 (French et al., 2013). (c) Average V_{SV} Pacific profiles from Nishimura and Forsyth (1989). (d) Regional studies are as follows: 0–10 Myr GLIMPSE (Harmon et al., 2009); 15 – 30 Myr Shikoku Basin (Takeo et al., 2013); 0 – 40 Myr PI-LAB (Harmon et al., 2020); and 70 Myr NoMelt (Lin et al., 2016).

being the cooling plate model (Parsons and Sclater, 1977; Stein and Stein, 1992). The physical mechanism behind the additional heat is debated, but it could be due to small scale convective instabilities (Richter, 1973) or the influence of plumes (Crough, 1983; Korenaga and Korenaga, 2008).

2.1. Thickness of the oceanic lithosphere

One might expect the thickness of the oceanic lithosphere to be less debated than that of the continents, given the previously discussed predictions for its evolution with age and also the fact that it is thinner, so there is less of a possible range for debate. Surface wave tomography provides an estimate of absolute shear velocity, which is useful for considering lithospheric thickness. Surface waves image a high velocity lithosphere that gets higher velocity and thicker with age, as predicted for a cooling plate (Fig. 2, 3). This is true in many studies in which data is binned by age (e.g. Nishimura and Forsyth, 1989; Ritzwoller et al., 2004; Priestley and McKenzie, 2006; James et al., 2014; Rychert et al., 2018a; Godfrey et al., 2017; Ma and Dalton, 2019; Beghein and Goes, 2019), and suggests that to first order temperature is a dominant factor in determining lithospheric seismic velocities and also the LAB, given the strong dependence of viscosity on temperature. However, individual cross-sections and higher resolution in situ imaging also show much more variability than simple monotonic increases in velocity and thickness (Fig. 2; Harmon et al., 2020; French et al., 2013). This could either be real or an artefact of the resolution of the tomography. In addition, the gradual character of the gradients in both predicted temperature and seismic velocity adds ambiguity in determining the exact depth of the transition from the lithosphere that moves relatively coherently to the convecting asthenosphere.

One challenge in tightly constraining the thickness of the oceanic lithosphere is that global seismic studies have low resolution at the shallowest depths where most of the variability related to oceanic lithospheric thickness occurs. Therefore, the exact shapes of the velocity profiles depend somewhat on assumptions, such as the smoothing, damping, starting model, and crustal structure. Regional studies that make in situ measurements have better vertical and horizontal resolution (Fig. 3d). However, comparisons between regional studies are challenging both because there have been very few broadband ocean bottom experiments, and also because the exact details of the seismic models vary according to the model assumptions in the given study.

The difficulty in resolving the plate is demonstrated by considering a simple exercise in which the lithosphere and the asthenosphere are determined by the highest and the lowest mantle velocities. With this definition, the lithosphere would be 0-30 km thick for young lithosphere (0-10 Myr) and 25-75 km thick for old lithosphere (100-170 Myr) in the global full-waveform model SEMum2 (Fig. 3) (French et al., 2013), whereas it would be 10-60 km thick for young lithosphere (0-4 Myr) and 50-150 km thick for old lithosphere ($>$ 110 Myr) in the surface wave model for the Pacific from Nishimura and Forsyth (1989). Overall, large uncertainties in oceanic plate thickness based on seismic wave velocities are difficult to avoid given large error bars on the velocity-depth profiles from tomography (Beghein and Goes, 2019).

Another approach to measuring lithospheric thickness is to consider the depth of the greatest negative velocity gradient. For instance, using this criteria Nishimura and Forsyth (1989) report LAB depths of 15-35 km for 0-4 Myr lithosphere and 70-110 km for lithosphere $>$ 110 Myr old. While this method provides a single or at least narrower depth estimate, values will vary by study according to the damping and smoothing assumptions of the model. For example, in the SEMum2 model (French et al., 2013) the sharpest gradients are at the surface of the Earth in younger lithospheric bins, reaching 46 km in the oldest age bin (Fig. 3).

An alternative for determining the depth of the LAB is to relate seismic velocities to temperature. A common choice is to find a isotherm that follows the transition from the high velocity lithosphere to the low velocity asthenosphere, and typically this corresponds to roughly the 1100°C isotherm (e.g. Ritzwoller et al., 2004). Several others have taken the approach of defining empirical relationships between velocities and temperatures predicted for a thermal model of the oceans (Priestley and McKenzie, 2006; Steinberger and Becker, 2018) in some cases including calibrations using xenoliths (e.g. Priestley and McKenzie, 2006). In these cases the LAB is then determined by the geotherm-adiabat intersection, i.e., the depth at which the dominant mode of heat transfer transitions from conduction to convection in thermal geodynamic models. Steinberger and Becker (2018) concluded that many models based on surface waves are well-correlated, regardless of their underlying assumptions or approaches, and also found a LAB around the ~1100°C isotherm. The attraction of this approach is that it gives a single depth for the LAB, rather than the more complex gradual transitions described above. However, it also assumes that a thermal model is necessarily correct, without accounting for chemical variability and/or the presence of melt.

Global models of seismic azimuthal anisotropy (variation in velocity with azimuth), typically based on the directional velocity dependence of Rayleigh waves, have also been employed to determine the LAB depth in oceanic settings. The fast direction of azimuthal anisotropy is often thought to be due to olivine crystals aligned with mantle deformation produced by shear due to plate translation. These studies typically find shallow azimuthal anisotropy fast directions that reflect past plate motions and/or deeper azimuthal fast directions in the direction of present-day absolute plate motion or sub-parallel to it (Maggi et al., 2006; Debayle and Ricard, 2012; Burgos et al., 2014; Beghein et al., 2014; Schaeffer and Lebedev, 2015). The transition between the shallow and deeper domains is typically interpreted as the LAB, although exact depth resolution of the transition and/or variability with age is challenging given the broad depth sensitivity of the waveforms.

Radial anisotropy (variation in velocity that depends on seismic propagation or polarization in the horizontal vs. vertical plane), typically based on the comparison of Rayleigh and Love wave dispersion, has also been used to distinguish the LAB. The typical assumption is that fast horizontal velocities reflect strong olivine alignment associated with mantle deformation in the convecting asthenosphere caused by present-day plate motions. Therefore, a peak in radial anisotropy at depth has been interpreted as the fully deforming asthenosphere (Montagner, 2002; Gung et al., 2003; Nettles and Dziewonski, 2008). However, it has also been suggested that an increase in radial anisotropy is not necessarily related to the LAB, and could instead represent a feature within the lithosphere, at a relatively constant depth (Burgos et al., 2014; Auer et al., 2015). One problem is that the depth resolution of radial anisotropy is poor given the different shapes of the sensitivity kernels of Love and Rayleigh waves (Rychert and Harmon, 2017). A second challenge is the difficulty of isolating the fundamental-mode Love wave from interfering overtones, which is especially problematic in regional-scale studies (Foster et al., 2014a).

Scattered wave imaging is an effective way to achieve constraints on velocity discontinuities potentially related to the LAB, in particular P-to-S (Ps) and S-to-P (Sp) receiver functions. However, receiver function observations are much more rare beneath the oceans than beneath the continents owing to a comparatively small number of seismic data from broadband ocean bottom instruments and also the fact that calculating receiver functions using ocean bottom data can be challenging due to noise and contamination from the water column and/or sediment reverberations (e.g. Reeves et al., 2015; Olugboji et al., 2016; Rychert et al., 2018b). Active source reflection experiments give the highest resolution, although the equipment required to reach the LAB beneath the oceans (e.g. Stern et al., 2015; Mehouachi and Singh, 2018), such as long streamers and large sources, is not typically available for academic use. Observations from SS underside reflections by themselves or in combination with other waveforms give good lateral coverage over the oceans and in particular the Pacific, without the need for ocean bottom seismic instrumentation (e.g. Rychert and Shearer, 2011; Schmerr, 2012; Tharimena et al., 2017a). However, these phases also have a wide

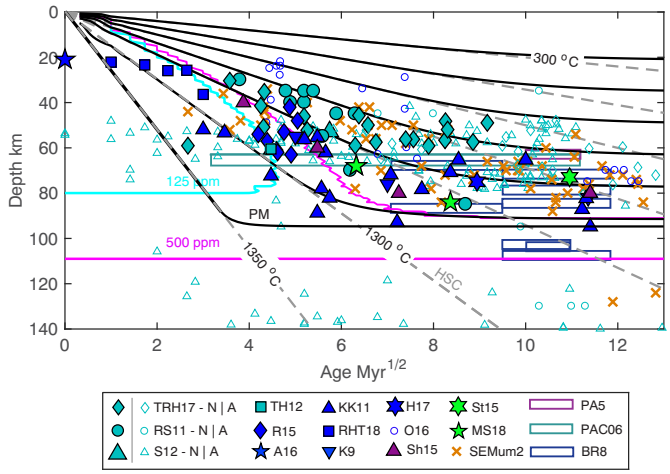

Fig. 4. Compiled discontinuity depths from scattered/reflected waves and other seismic methods plotted versus age compared to cooling model predictions and surface wave velocities. Isotherms for the half-space cooling model (HSC; gray dashed) and plate model assuming plate thicknesses of 95 km (PM; black solid) are shown. Isotherms are plotted every 200 °C and including an isotherm very near the mantle potential temperature of 1350 °C. The solidi for a mildly hydrated mantle are shown for 125 ppm and 500 ppm water (cyan and pink lines, respectively) (Katz et al., 2003). Depths are plotted relative to the seafloor with results corrected from the depth beneath sea surface by the amount listed, if any. SS precursor results from the entire Pacific including TRH17 (Tharimena et al., 2017a, b), RS11 (Rychert and Shearer, 2011), and S12 (Schmerr, 2012) are sorted into normal lithosphere (N, solid cyan) and anomalous (A, outline cyan) lithosphere affected by hotpots (Korenaga and Karato, 2008). Depths from a sS precursor result, TH12 (Tonegawa and Helffrich, 2012) (cyan star), and a Po/So result, Sh15 (Shito et al., 2015) (purple triangle), are shown. Receiver function results (solid blue symbols) include RHT18 (Rychert et al., 2018b) (−3 km), R15 (Reeves et al., 2015) (−3 km), O16 (Olugboji et al., 2016), KK11 (Kumar and Kawakatsu, 2011), K9 (Kawakatsu et al., 2009), H17 (Hannemann et al., 2017), and A16 (Audet, 2016). Transect studies that encompass a range of ages are shown as boxes with fixed thickness (5 km), including PAC06 (Tan and Helmberger, 2007) (green), PA5 (Gaherty et al., 1996) (−5 km) (purple), and BR08 (Bagley and Revenaugh, 2008) (−4 km) (blue). Active source studies (solid green symbols) include MS18 (Mehouachi and Singh, 2018) (−4 km) and St15 (Stern et al., 2015).

zone of lateral sensitivity, with potential difficulty imaging discontinuities at variable depths.

We present a global compilation of oceanic velocity discontinuities or gradients based on Ps and Sp receiver functions, SS precursors, and active source reflections, as well as guided waves and transect studies that use SS or ScS bounces in combination with other phases. For three Pacific-wide SS precursor studies (Rychert and Shearer, 2011; Schmerr, 2012; Tharimena et al., 2017a) bins located on normal oceanic lithosphere are shown as solid symbols, whereas bins on or nearby hotspots, or in undefined regions (Korenaga and Korenaga, 2008), are shown as open symbols. Considering only the bins from normal oceanic lithosphere in the latter three studies, the data show a pattern of increasing discontinuity depth with seafloor age beneath young ($<\sim$6 Myr$^{1/2}$) lithosphere with a broad distribution of depths (40-90 km) beneath older ($>\sim$6 Myr$^{1/2}$) lithosphere (Fig. 4). Beneath the youngest lithosphere ($<$2 Myr$^{1/2}$) the observations are deeper than the thermal contours of half-space cooling. This result is explained by the fact that half-space cooling assumes one-dimensional heat conduction, not accounting for lateral heat conduction. While lateral heat conduction is not predicted to play a large role at fast spreading ridges like the East Pacific Rise, the effect is predicted to be more pronounced for slower spreading ridges, creating thickened lithosphere beneath the ridge axis (Morgan et al., 1987). The anomalously deep cases at very young ages in Fig. 4 come from slower spreading regions, including Cascadia (intermediate spreading) and the Mid-Atlantic Ridge (slow spreading). The discontinuity depths then roughly follow the 1100° C isotherm until ~6-8 Myr$^{1/2}$ before flattening to scattered depths centered around 60 km depth. The general agreement with isotherms suggests that temperature plays a role in the depths of the discontinuities. The discontinuity depths also generally fall within the gradual decreases in shear velocity observed in some surface wave tomography models and/or they align with the lowest asthenospheric velocities, for example in the SEMum2 model (French et al., 2013) (the orange crosses in Fig. 4). Therefore it has been suggested that these converted and reflected waves are imaging the lithosphere-asthenosphere boundary, for example where the LAB is defined by the 1100° C isotherm for the cooling plate model (Fig. 4), putting tight constraints on its depth. There are also a number of arguments against this, which we discuss below.

2.2. Sharpness of the oceanic lithosphere-asthenosphere transition

For the classic thermally defined oceanic lithosphere, the transition from the rigid lithosphere to the weaker asthenosphere will occur gradually in depth. In other words, as temperature increases with depth, the mantle also gets weaker, deforming, and finally fully convecting at the geotherm-adiabat intersection. The predicted and observed seismic velocity profiles for young lithosphere define a velocity gradient that occurs over 50 km, in contrast to a much greater depth range (140-150 km) for the oldest lithosphere (Fig. 3a, c). The predicted total drop in velocity from the lithosphere to the asthenosphere is also more muted beneath the oldest seafloor, relative to that at intermediate ages.

Scattered wave observations require discontinuities that are much sharper, on the order of 7-8% over less than 10-15 km (Kawakatsu et al., 2009), than those predicted for the thermal models and also those constrained by surface waves. Some active source experiments hypothesize that there could be even sharper (<1 km) LAB-related discontinuities, at the top and bottom of ~8% low velocity channels beneath the plate (Stern et al., 2015; Mehouachi and Singh, 2018). Given that the depths of the scattered wave discontinuities agree with predictions for the LAB, for example as defined by the 1100° C isotherm (e.g. Fig. 4), it has also been suggested that the LAB beneath the oceans is sharp. This conclusion would not necessarily be inconsistent with the surface wave observations. Surface wave sensitivity kernels are broad in depth and therefore cannot distinguish between sharp velocity gradients and those that occur over tens of kilometers. It is also not necessarily inconsistent with the notion that temperature is an important factor in the evolution of oceanic lithosphere, for example controlling the depth of the observed discontinuities as described above.

Several sub-solidus mechanisms have been proposed to create sharp vertical velocity gradients that could explain the scattered wave observations. For instance, variations in chemical depletion could be sharp. Also, a frozen-in pyroxenite melt could be up to ~13.6 % slower than a lherzolite matrix, potentially resulting in a strong velocity contrast (Hacker et al., 2003; Rychert and Harmon, 2017) if the frozen-in melt were pervasive over hundreds of kilometers laterally and tens of kilometers in depth. However, typically the scale of very high degree melting required to create a pyroxenite melt is thought to be small. Extreme changes of 10 orders of magnitude in grain size or hydration are only predicted to give a 3% velocity contrast (Behn et al., 2009). Elastically accommodated grain boundary sliding has been proposed as a mechanism to enhance the effect of hydration on seismic waves (Karato, 2012; Olugboji et al., 2013), potentially creating a discontinuity that could be related to the rheologic lithosphere-asthenosphere transition given the weakening effect of water on viscosity. Ma et al. (2020) have invoked elastically accommodated grain-boundary sliding to explain the moderate attenuation and low shear velocity observed in the depth range of 70-200 km at the NoMelt array of ocean bottom seismometers on 70-Myr Pacific seafloor. However, predictions for the elastically accommodated grain-boundary sliding model include an increase in the sharpness of the seismic velocity discontinuities with age that is not supported by some seismic imaging results (Rychert et al., 2018a). The

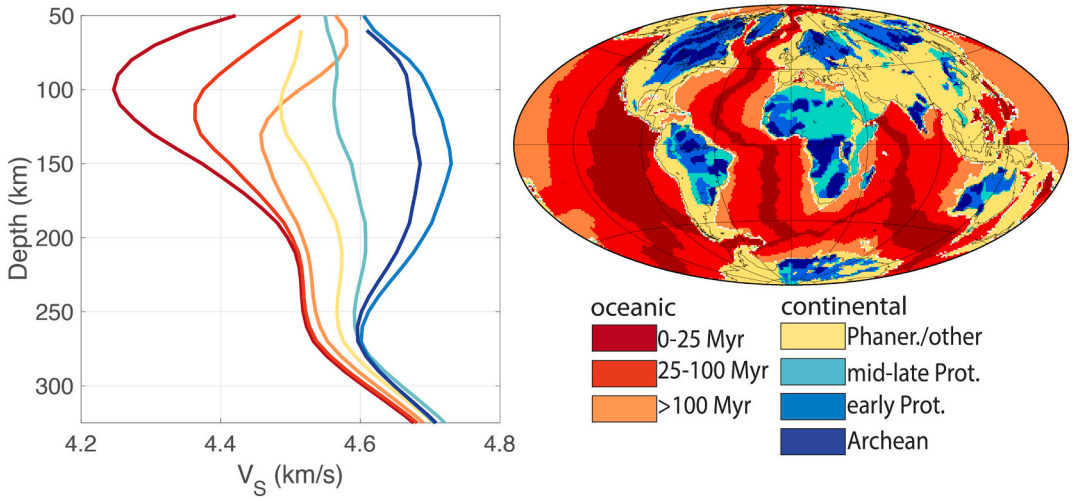

Fig. 5. left) Velocity (V_{sv}) profiles from the SEMum2 model (French and Romanowicz, 2014). Each profile corresponds to a global average of mantle structure beneath crust of a given age. right) Age classification of crust from the Crust1.0 model (Laske et al., 2013). Ages on map and for velocity profiles are color-coded according to the legend in the lower right.

pre-melting effect observed in the laboratory by Yamauchi and Takei (2016) predicts a large velocity reduction at sub-solidus conditions, although the expected depths and amplitudes of the resulting velocity gradients are still insufficient to explain the scattered wave observations (Rychert and Harmon, 2018). Finally, changes in radial or azimuthal anisotropy internal to the lithosphere have been proposed (Beghein et al., 2014; Auer et al., 2015), although neither compositional layering nor radial anisotropy resulting from either random or sub-Fresnel-zone alignment of olivine in the horizontal plane can explain receiver function velocity contrasts of greater than 2% or consistently negative velocity contrasts among methods (Rychert and Harmon, 2017).

Another possibility is that partial melt in the mantle plays a role in the seismic observations. While the presence of melt is not required to explain isotropic wave velocities imaged with surface waves in the presence of strong attenuation, the attenuation required would need to be stronger than observed, necessarily requiring a factor besides temperature (Goes et al., 2012; Beghein and Goes, 2019). Another mechanism is also required to explain the sharpness of the seismic velocity discontinuities observed with converted and refelected body waves (e.g. Kawakatsu et al., 2009; Rychert et al., 2019). The amount of melt required to explain the seismic observations (<1%) (Hammond and Humphreys, 2000; Chantel et al., 2016) or more (Clark and Lesher, 2017) would also significantly reduce the viscosity of the mantle (Hirth and Kohlstedt, 1995; Jackson et al., 2006), enabling it to convect and defining the lithosphere-asthenosphere boundary (Rychert et al., 2005). Indeed, observational constraints on asthenospheric low viscosity are as low at 10^18 Ps, an order of magnitude lower than predictions from some geodynamic models (Rychert et al., 2020; refs. therein). Low asthenospheric viscosities play a key role in decoupling deformation in the deeper mantle from plate motions, altering predictions of azimuthal anisotropy (e.g. Becker, 2017).

The concept of melt collected below the LAB, in large enough quantities to produce the velocity decreases indicated by scattered and reflected phases, raises the question of how melt could be stable at these depths over wide regions of the oceanic mantle. In one model, Sakamaki et al. (2013) estimated the mobility of partial melt, defined as the ratio of the density contrast between melt and olivine to melt viscosity, and found that melt would tend to rise rapidly out of the asthenosphere, but then accumulate at the LAB due to lower mobility in the lithosphere. Alternatively, the base of the cold lithosphere may represent a permeability barrier to rising melt, producing a melt-rich boundary layer just beneath (e.g. Sparks and Parmentier, 1991; Wang et al., 2020). While even modest topography on this type of boundary drives melt along the layer towards shallower depths, for example focusing melt to mid-ocean ridges (e.g. Sparks and Parmentier, 1991; Sim et al., 2020), continued upwelling of mantle and melt would provide a steady-state source of melt. However, the association of upwelling asthenosphere, melt generation, and converted/reflected detections of the LAB remains unclear. Clerc et al. (2018) did not find a significant correlation between upwelling velocities in a global flow model and the Schmerr (2012) SS precursor LAB detections from depths less than 80 km, and did not resolve a correlation when the SS precursor results of Tharimena et al. (2017a) were considered. However, Clerc et al. (2018) point out that convection at scales smaller than resolved in their flow model may be an alternative source of partial melt. Intriguingly, they did find a correlation between upwelling velocities and velocity decreases from SS precursors at depths greater than 80 km, suggesting that these deeper interfaces may be related to the transition between carbonate melting and carbonate combined with water-enhanced silicate melting. As shown in Fig. 4, these deeper interfaces do not lie in regions of normal oceanic lithosphere, as defined by Korenaga and Korenaga (2008), but rather near hotspots, consistent with correlation to upwelling mantle, or in undefined zones.

2.3. *Structures internal to the oceanic mantle lithosphere*

While seismic models determined from surface wave phase velocities generally agree regarding the presence of a seismically fast lid, often assumed to correspond to the lithosphere, and an underlying seismically slower layer, associated with the asthenosphere, and while many scattered wave studies detect a sharp discontinuity that may correspond to the LAB, seismic imaging of the internal velocity structure of the oceanic lithosphere has proven challenging, primarily owing to the difficulty in resolving structure at these depths in remote locations. Some studies have observed high frequency, large amplitude coda from earthquakes that originate within subducted slabs (e.g. Furumura and Kennett, 2005; Shito et al., 2013; Sun et al., 2014) and are recorded at seismic stations above the subduction zone. These types of seismic signals have been suggested as the product of small-scale heterogeneities in the oceanic lithosphere. In addition, one active source study on old (148-128 Myr) Pacific lithosphere found several wide angle reflections consistent with individual 2 km thick low-velocity (7% slow) zones at 37-59 km depth. These were interpreted as melt pockets that were frozen into the lithosphere as it formed, possibly related to the heterogeneity that created the coda described above, and referred to as mid-lithospheric discontinuities (MLDs) (Ohira et al., 2017). Overall, given a lack of

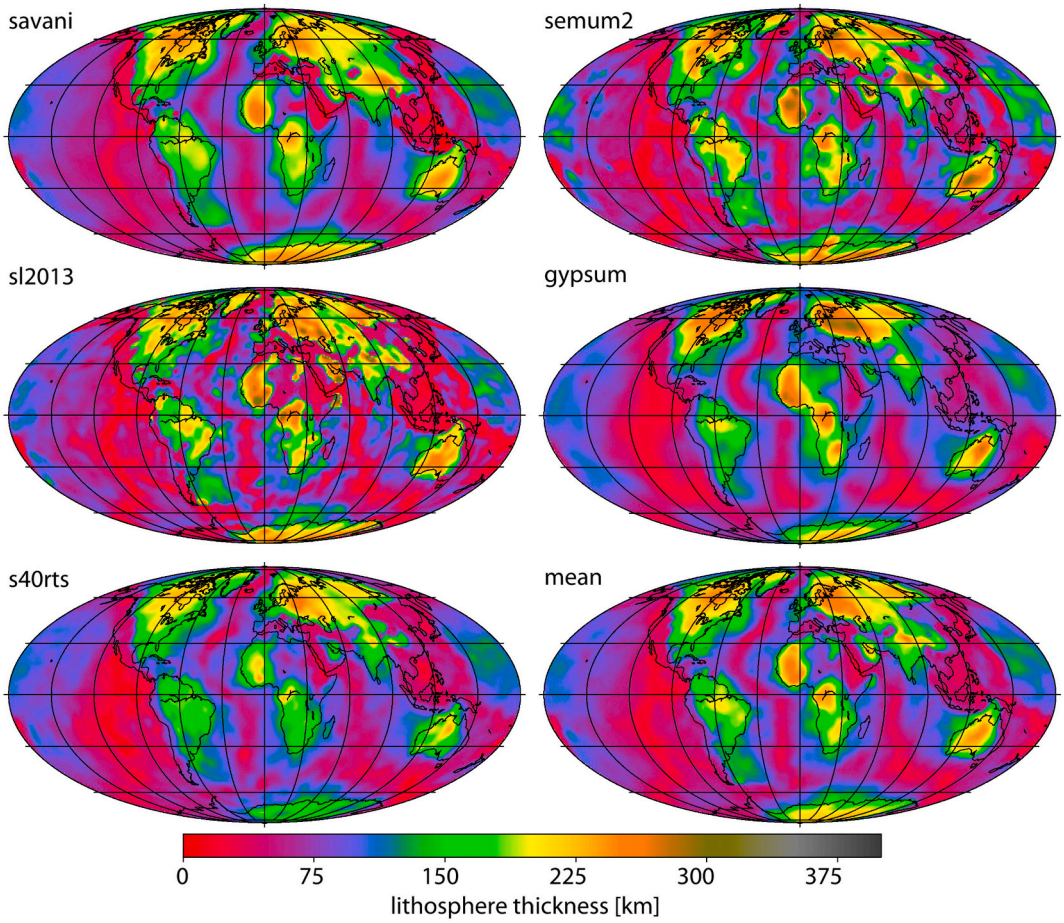

Fig. 6. From Steinberger and Becker (2018). Maps of the thermal thickness of the lithosphere based on different global tomography models: gypsum (Simmons et al., 2010), s40rts (Ritsema et al., 2011), savani (Auer et al., 2014), SEMum2 (French and Romanowicz, 2014), and sl2013 (Schaeffer and Lebedev, 2013). The mean model is an average of these five models.

comprehensive high resolution constraints, the detailed physical properties of these heterogeneities are not well constrained.

3. Continental lithosphere

In contrast to the relatively simple life-cycle of the oceanic lithosphere, continental lithosphere contains the time-integrated record of a complex range of tectonic events: plate collisions, plate break-up, modification due to subduction zone processes, interactions with mantle plumes, and more. Hence the properties of the continental lithosphere are not expected to follow monotonic thermal histories, such as those explored in relation to the oceanic lithosphere in the preceding section.

3.1. Cratonic versus phanerozoic continental lithosphere

A first-order feature of the continental upper mantle is that seismic velocities are higher and attenuation is lower beneath cratonic regions – zones that have not experienced widespread tectonic activity and/or magmatism since the end of the Proterozoic – compared to continental regions that were accreted, rifted or otherwise reworked during the Phanerozoic. For example, this contrast is expressed clearly in global models of shear-wave velocity at a depth of 150 km (Fig. 1). Beneath Proterozoic and Archean cratons, shear velocities are up to 8% higher than the global average for that depth. Another way to express this contrast is to average depth profiles of absolute shear-wave velocity within regions of a particular age. For example, in Fig. 5 the Earth is divided using the age classification of the Crust1.0 crustal model (Laske et al., 2013), and V_{sv} values from the SEMum2 model (French et al., 2013; French and Romanowicz, 2014) are averaged at a given depth for all points within a particular age zone. Among continental regions, the V_{sv} profiles for mantle beneath early Proterozoic and Archean crust (the two darkest blues) have the highest velocities at depths of 50-250 km, and the V_{sv} values for mantle beneath Phanerozoic crust (yellow) are significantly lower.

A variety of other geophysical and geochemical observations also differ between cratonic lithosphere and the lithosphere in Phanerozoic continental regions. In cratons, surface heat flows are low (e.g. Pollack et al., 1993; Rudnick and Nyblade, 1999; Mareschal and Jaupart, 2004), and these observations combined with xenolith data and high seismic velocities indicate that cratons are underlain by thick layers of cold mantle that have been highly depleted by melt extraction (e.g. Jordan, 1978; Boyd, 1989; Griffin et al., 1999; Lee, 2006; Lee et al., 2011). While a melt depleted harzburgitic cratonic mantle was initially thought to be the source of higher cratonic velocities (Jordan, 1978), careful examination of melt extraction effects from laboratory measurements and thermodynamic models shows a very muted effect on velocities (e.g. Schutt and Lesher, 2006; Afonso et al., 2010; Afonso and Schutt, 2012), leading to the suggestion that high cratonic velocities may be due to other compositional factors (e.g. Dalton et al., 2017; Garber et al., 2018), as discussed in Section 3.4. Much of the cratonic mantle has remained stable over billions of years (e.g. Richardson et al., 1984; Pearson et al., 1995) likely aided by a roughly neutral buoyancy and high viscosity (e.g. Shapiro et al., 1999; Perry et al., 2003; Sleep, 2005; Cooper and Miller, 2014). The absence of a high velocity mantle root beneath a few cratons, such as the eastern North China craton (e.g. Xu

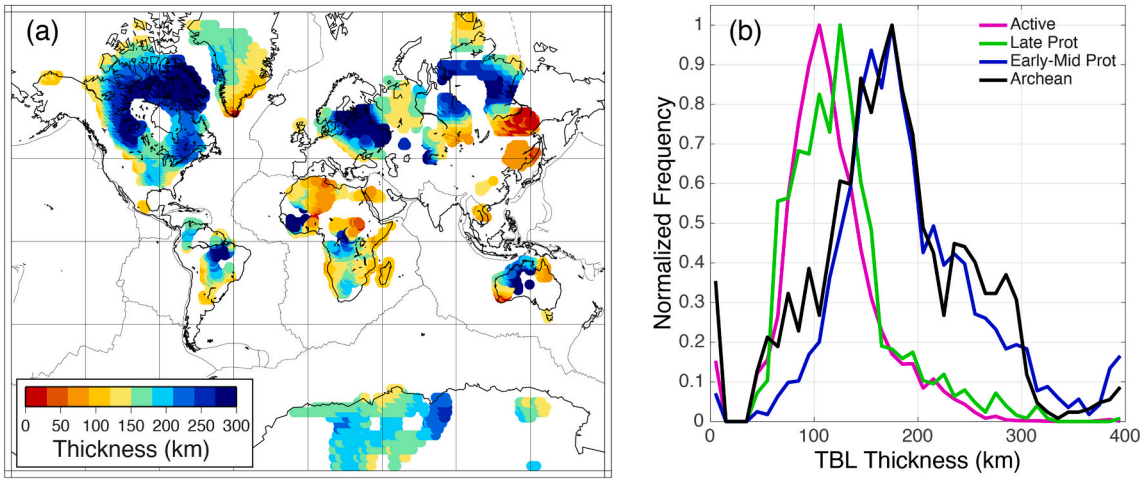

Fig. 7. From Dalton et al. (2017). a) Map of thermal boundary layer thickness determined from global Rayleigh wave attenuation data for the continental lithosphere in regions of Archean and Proterozoic crust. Blank regions correspond to either younger crust or to Precambrian regions where fits between thermal models and attenuation structure did not meet misfit criteria. b) Distributions of thermal boundary layer (TBL) thickness globally averaged for different crustal ages.

and Zhao, 2009; Wu et al., 2019) and the western Wyoming craton (e.g. Porritt et al., 2014; Schaeffer and Lebedev, 2014; Schmandt et al., 2015; Shen and Ritzwoller, 2016), is often interpreted as evidence for the destruction of the deep mantle lithosphere in these regions. Mechanisms for removal or replacement of thick cratonic lithosphere include its interaction with low angle subducting lithosphere (e.g. Snyder et al., 2017; Wu et al., 2019) or mantle plumes (e.g. Hu et al., 2018), or dynamic instability due to weak internal layers (e.g. Snyder et al., 2017; Liu et al., 2018; Hu et al., 2018).

3.2. *The thickness of the continental lithosphere*

The thickness of the continental lithosphere is a much-debated question, with widely varying answers even in a single region depending on the criteria used to define the lithosphere-asthenosphere transition. A simple definition is to say that the highest absolute velocities must lie in the colder mantle of the lithosphere, and the lowest absolute velocities must lie in the warmer, weaker asthenosphere. However, applying this criterion to the SEMum2 absolute velocity profiles in Fig. 5 yields very wide bounds on average lithospheric thicknesses: 150 km to 260 km beneath early Proterozoic and Archean cratons and 60 km to 110 km in Phanerozoic regions. Note that the average lithospheric thicknesses measured for Phanerozoic continental regions (yellow V_{sv} profile in Fig. 5) are comparable to lithospheric thicknesses estimated for middle-aged (25 Ma to 100 Ma) oceanic lithosphere (bright red V_{sv} profile in Fig. 5). However, this global average for Phanerozoic continents includes a diverse range of lithospheric structure, ranging from portions of the Basin and Range of the U.S. and the East African Rift system where the high velocity lithospheric mantle lid is only 10-30 km thick, or not present at all, to older Phanerozoic lithosphere, such as the Appalachian orogen, where lithospheric mantle of 60-80 km in thickness is not uncommon (e.g. Weeraratne et al., 2003; Adams et al., 2012; Porritt et al., 2014; Schaeffer and Lebedev, 2014; Schmandt et al., 2015; Shen and Ritzwoller, 2016; Wagner et al., 2018). Alternative strategies include defining the base of the lithosphere by the maximum negative gradient within the broad zone of velocity decrease defined above, or choosing a particular velocity contour. However, these approaches are highly dependent on the details of specific velocity models, and their application to a range of models often produces discrepancies in lithospheric thickness estimates.

Another approach is to define the base of the lithosphere as the depth where the profiles converge. For example, the SEMum2 cratonic profiles (Fig. 5) converge with each other at a depth of ~260 km, but the continental and ocean profiles converge at greater depths. Jordan and Paulson (2013) applied this type of analysis to a range of global models and found convergence of cratonic and oceanic profiles occurs at depths greater than 350, leading them to infer that a coherent mantle layer ("tectosphere") extends nearly to the 410 km discontinuity. An alternative explanation is that variations in absolute V_s persist into the asthenosphere, produced by temperature or possible compositional heterogeneity.

A different strategy is to fit observed velocity or attenuation profiles with profiles predicted by thermal models for the continental lithosphere, and to then define the base of the lithosphere as the depth where the conductive portion of the geotherm intersects a mantle adiabat (e.g. Priestley and McKenzie, 2013; Plank and Forsyth, 2016; Steinberger and Becker, 2018; Dalton et al., 2017; Cammarano and Guerri, 2017) (Figs. 6 and 7). Since seismic velocities vary more strongly with bulk composition than does seismic attenuation, estimates of lithospheric temperature and thickness based on attenuation (e.g. Dalton et al., 2017) are less subject to assumptions about composition. Attenuation-based estimates of lithospheric thermal thickness are significantly larger beneath early to mid-Proterozoic and Archean crust than beneath late Proterozoic and younger continental crust (Fig. 7), in agreement with the age-averaged velocity profiles in Fig. 5.

Anisotropy in seismic velocities is also a powerful tool for assessing the thickness of the continental lithosphere. Lithospheric thicknesses have been estimated using vertical variations in both radial (e.g. Gung et al., 2003) and azimuthal anisotropy (e.g. Debayle and Kennett, 2000; Yuan and Romanowicz, 2010; Yuan and Beghein, 2013, 2014). By constraining radial anisotropy at the global scale from three-component long-period seismograms, Gung et al. (2003) found that horizontally polarized shear waves travel faster than vertically polarized shear waves under most cratons between 250 km and 400 km depth. They proposed that this signal was the signature of olivine crystals aligned within a low viscosity asthenospheric channel and therefore that the top of that layer delimits the cratonic LAB. Measures of lithospheric thickness based on azimuthal anisotropy have been obtained from surface wave dispersion studies and long-period seismogram inversions. As described above for the oceans, assuming that the fast direction of azimuthal anisotropy is due to olivine crystals aligned with mantle deformation, and that mantle deformation in the shallow asthenosphere is produced by shear due to plate translation, lithospheric thickness can be defined as the depth where azimuthal anisotropy rotates into the direction of present-day absolution plate motion (e.g. Debayle and Kennett, 2000; Yuan and Romanowicz, 2010; Yuan and Beghein, 2013, 2014). This approach has led to values for continental lithosphere thickness of 180-240 km for cratons (Yuan and Romanowicz, 2010; Yuan et al., 2011; Yuan and

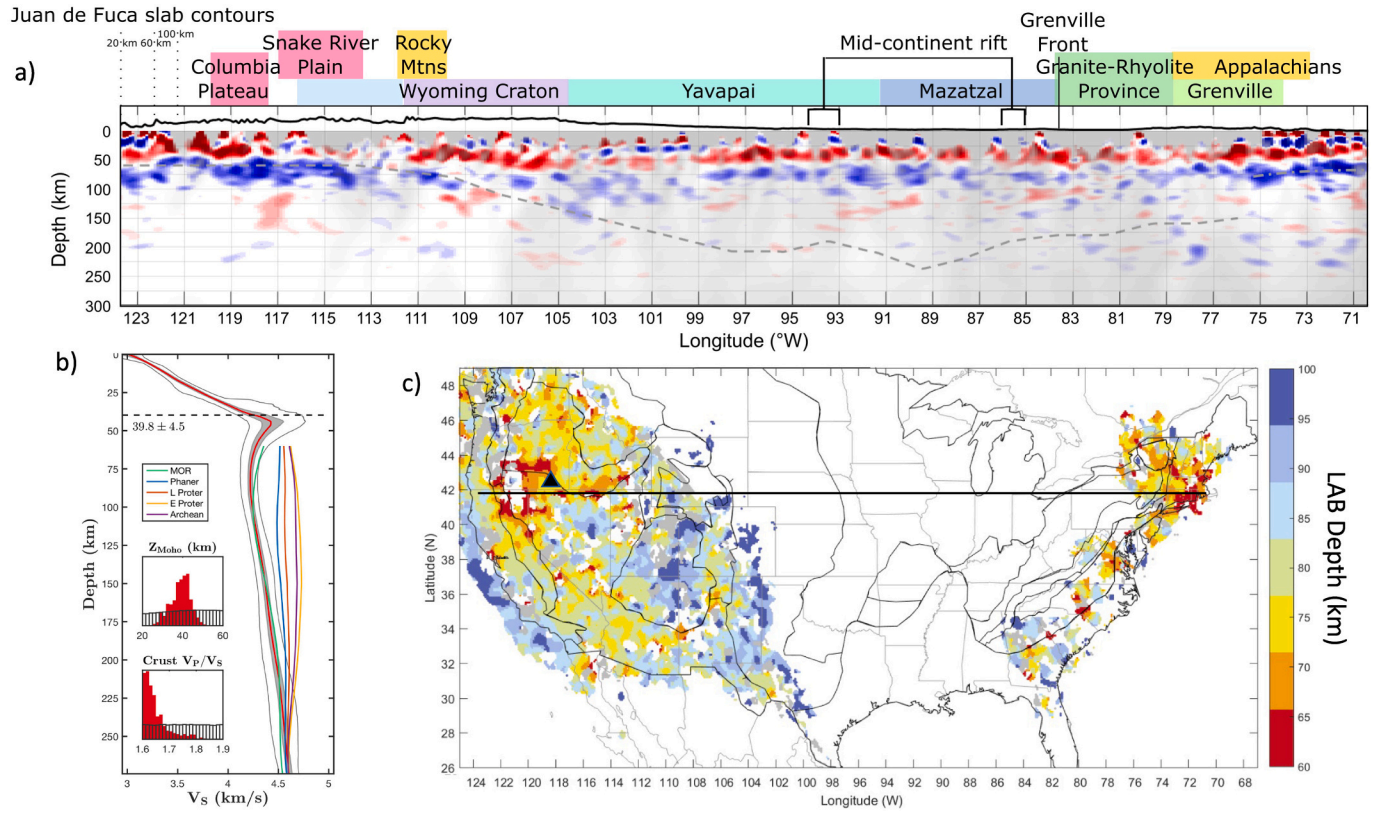

Fig. 8. a) After Hopper and Fischer (2018). E-W profile across the U.S. at 41.8°N showing the mean of a bootstrapped Sp common conversion point stack (4-100 s). Grey dashed lines: LAB estimate from Cammarano and Guerri (2017) geotherms, where the base of the lithosphere is defined by the contour at 1132°C (as in Steinberger and Becker, 2018). The eastern margin of thick cratonic lithosphere was estimated from regional tomography (Wagner et al., 2018; Pollitz and Mooney, 2016). East of this point a dot-dashed grey line marks possible LAB depth from the Sp CCP stack. Grey overlay grades from completely transparent to completely opaque with decreasing $\log_{10}$(sampling). Cross sections are plotted at 2x vertical exaggeration. Topography is plotted at 10x vertical exaggeration. b) After Eilon et al. (2018). Shear-velocity model for station WVOR in Oregon, obtained by transdimensional hierarchical Bayesian inversion of Rayleigh wave phase velocities and Sp and Ps converted waves. Red lines: average model. Grey lines: 2σ bounds. Insets show posterior (red) versus prior (white) estimates for Moho depth and crustal V_P/V_S ratio. Overlaid lines show shear velocities from global model SEMum2 (French et al., 2013) averaged by age of the continental crust (Phanerozoic, Late Proterozoic, Early-Mid Proterozoic, Archean) and beneath 0-25 Myr seafloor. c) From Hopper and Fischer (2018). Colors indicate the depth of the LAB velocity gradient measured from the Sp common conversion point stack. The LAB depth is defined as the deepest local Sp phase indicative of a negative velocity gradient with depth, if that velocity gradient is within 20 km depth of the tomographically estimated LAB depth (Cammarano and Guerri, 2017; Wagner et al., 2018). Black line shows the location of the profile in (a). Black triangle shows the location of station WVOR in (b).

Beghein, 2014) and 70-80 km in more tectonically active regions such as the western United States (Yuan et al., 2011). However, as pointed out by Debayle and Kennett (2000), the mechanical thickness of the lithosphere, as defined by rotation of azimuthal anisotropy into the direction of asthenospheric shear, may differ from the compositional or thermal thickness of the lithosphere.

While inversions that include surface wave data typically have better vertical resolution of upper mantle shear-wave velocities than that provided by teleseismic body-wave data, surface waves alone have very limited ability to distinguish between vertical velocity gradients that are distributed over several tens of kilometers in depth, and those that occur instantaneously in depth (i.e. a step function in depth) (e.g. Eaton et al., 2009). As previously discussed, converted phases (e.g. Sp and Ps) and reflected phases (e.g. SS precursors and ScS reverberations) have greater sensitivity to the depth and depth extent of lithosphere-asthenosphere velocity gradients, and in recent years rapid growth in analyses of converted and reflected waveforms has occurred for the continents (e.g. Bostock, 1998; Rychert et al., 2005; Yuan et al., 2006; Rychert and Shearer, 2009; Eaton et al., 2009; Fischer et al., 2010; Fischer, 2015; Cooper et al., 2017; Tharimena et al., 2017b; Hua et al., 2018; Shearer and Buehler, 2019; Hua et al., 2020). For example, common conversion point stacking of Sp phases in the northwest U.S. revealed a negative velocity gradient at depths of 65-75 km beneath the northern Basin and Range and High Lava Plains region of the western U.S. (Fig. 8a and c) (Hopper et al., 2014; Hopper and Fischer, 2018). When the strong, coherent Sp phases from the shallow mantle of this region are jointly inverted with Rayleigh wave phase velocities, the Sp energy requires a much more rapid velocity decrease from 50 km to 75 km than would have been necessary if only the Rayleigh wave data were inverted (Eilon et al., 2018) (Fig. 8b).

The presence of seismic anisotropy has also been measured with converted body waves, for example using back-azimuthal variations in P-to-SV and P-to-SH conversions (e.g. Levin and Park, 1997; Bostock, 1998). This type of anisotropic receiver function analysis has been applied by different groups to detect sharp contrasts in anisotropic structure with depth within the crust (e.g. Porter et al., 2011; Schulte-Pelkum and Mahan, 2014) and within the lithospheric mantle (e.g. Bostock, 1998; Yuan and Levin, 2014; Wirth and Long, 2014; Ford et al., 2016). Using this technique together with SKS waveforms beneath eastern North America, Yuan and Levin (2014) were able to constrain the depth of the LAB at ~100 km. Their findings resulted from a change in seismic anisotropy between a lithosphere characterized by a fast axis orientation orthogonal to the strike of major tectonic units and an underlying asthenosphere with fast axis directions sub-parallel to present-day plate motion direction (Gripp and Gordon, 2002).

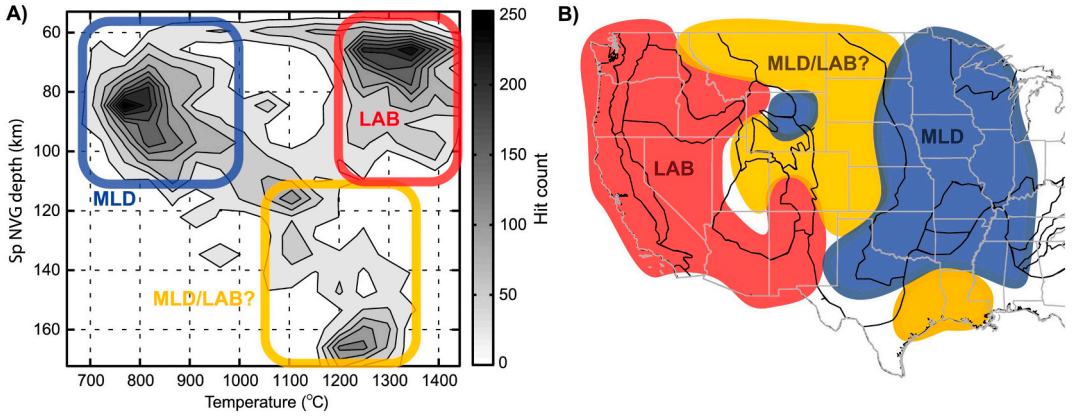

Fig. 9. From Hansen et al. (2015). Thermal classification of negative velocity gradients observed in a Sp receiver function stack. a) The mantle temperature (inferred from seismic velocities) at each negative velocity gradient pick is plotted as a depth–temperature histogram; thermal classifications are labeled. b) The approximate geographic distribution of the classified negative velocity depths in (a). The modal peak at 1345°C and 66 km depth is largely from the regions of thin lithosphere in the western U.S. and is interpreted as the LAB. The peak at 770°C and 84 km depth occurs in regions of thick lithosphere in the central U.S. and is interpreted as MLDs. A third smaller peak near 1230°C and 165 km depth is interpreted as deep MLDs beneath the northern Rockies and Plains.

3.3. *The sharpness of the continental lithosphere-asthenosphere transition*

As described earlier, the properties of the lithosphere-asthenosphere velocity gradient are key to discerning the physical and chemical properties that govern this transition. Velocity gradients produced by typical steady-state continental geotherms alone are predicted to occur over at least 60 km or more (e.g. Priestley and McKenzie, 2013; Dalton et al., 2017), vertical variations in Mg# or water as point defects in olivine can be sharp but are limited in magnitude, and partial melt can produce velocity reductions that are both sharp and large (>5%).

In studies that employ converted phases such as Sp and Ps, the lithosphere-asthenosphere transition beneath Phanerozoic continental regions is typically characterized by a significant velocity gradient that is localized over 30 km or less (for reviews see Rychert et al., 2010; Fischer et al., 2010; Kind et al., 2012; Fischer, 2015). For example, clear, large amplitude negative velocity gradients have been imaged in the shallow mantle across much of the Cordillera with Sp phases (e.g. Heit et al., 2007; Lekic et al., 2011; Levander and Miller, 2012; Kind et al., 2012; Hansen et al., 2013; Lekic and Fischer, 2014; Ford et al., 2014; Hopper et al., 2014; Hansen et al., 2015; O'Driscoll and Miller, 2015; Hopper and Fischer, 2018) (Figs. 8 and 9). Sp-derived negative velocity gradients observed beneath the High Lava Plains region (Fig. 8a), correspond to a velocity decrease of ~7% over 40 km in depth when jointly inverted with Rayleigh wave phase velocities (Fig. 8b) (Eilon et al., 2018).

The magnitude and sharpness of the lithosphere-asthenosphere velocity gradient appear to vary with likely asthenospheric partial melt content, but this behavior is not monotonic. Large, localized velocity gradients are often observed in regions that have recently experienced magmatic activity in the last 5-10 Myr (Ford et al., 2010; Levander and Miller, 2012; Hopper et al., 2014; Hansen et al., 2015; Miller et al., 2015). However, some zones of ongoing or very recent magmatism, such as the regions around the Yellowstone Hotspot, the Cascades arc, and portions of the Basin and Range that have experienced magmatism in the last few million years in fact have somewhat weaker negative LAB velocity gradients than their surroundings, suggesting that enough melt has infiltrated the lower lithosphere to erase much of the lithosphere-asthenosphere velocity contrast (Hopper et al., 2014; Hopper and Fischer, 2018). Going even further, beneath the Afar Rift in eastern Africa, a velocity increase is observed close to the rift axis, in contrast to negative velocity gradients beneath the rift flanks; the positive velocity gradient has been interpreted as the onset of partial melting (Rychert et al., 2012). In the Atlas Mountains in northwestern Africa, a very large magnitude velocity gradient occurs beneath portions of the range where recent basaltic magmatism has occurred (Miller et al., 2015), which is similar to some localized observations from Hopper et al. (2014) for the northwestern United States.

In contrast, lithosphere-asthenosphere velocity gradient properties beneath cratons are much less certain. Some studies have observed a typical absence of Sp or Ps energy, or at most only weak and intermittent phases, converted from the cratonic lithosphere-asthenosphere transition (Rychert and Shearer, 2009; Abt et al., 2010; Ford et al., 2010; Geissler et al., 2010; Kumar et al., 2012; Lekic and Fischer, 2014; Hopper et al., 2014; Hopper and Fischer, 2015; Knapmeyer-Endrun et al., 2017; Mancinelli et al., 2017; Hopper and Fischer, 2018). These results are consistent with negative lithosphere-asthenosphere shear velocity gradients that are comparable in strength and depth extent to those for Archean and mid to late-Proterozoic cratons in Fig. 5. However, other studies have inferred significant and widespread Sp and Ps phases from the base of the cratonic lithosphere, indicating more vertically localized gradients (Kumar et al., 2007; Wittlinger and Farra, 2007; Hansen et al., 2009; Miller and Eaton, 2010; Wölbern et al., 2012; Bodin et al., 2013; Kind et al., 2013; Sodoudi et al., 2013; Hansen et al., 2013; Foster et al., 2014b; Chen et al., 2014; Hansen et al., 2015; Calo et al., 2016; Kind et al., 2017; Kind and Yuan, 2019). Tharimena et al. (2017b) employed SS precursors to argue for the presence of a 7-9% velocity drop (typically over less than 30 km) at depths of 130-190 km beneath the cratons. However, this type of structure should produce strong Sp conversions, posing a puzzle for why such phases are not widely observed from the base of the cratonic lithosphere, particularly at long periods (Mancinelli et al., 2017).

Alternatively, autocorrelograms of P-wave reflectivity beneath a seismic station provide an image of the lithosphere at high resolution using higher frequencies than converted wave techniques. This method can aid in determining finer-scale structure and locations with velocity gradients. For example, within the Australian continent, autocorrelograms from vertical component data indicate a change of reflection character in the lower part of the lithosphere, which can be interpreted as the transition to the asthenosphere (Kennett, 2015; Kennett et al., 2017).

3.4. *Structures internal to the continental mantle lithosphere*

Boundaries and layers within the cratonic lithosphere have been imaged globally by several types of seismic observations. These include long-range refraction surveys (Thybo and Perchuc, 1997), P reflectivity (Sun and Kennett, 2017), ScS reverberations (Revenaugh and Jordan, 1991), regional P-wave waveforms (Chu et al., 2012), SS precursors

(Tharimena et al., 2017b), topside reflections of direct S phases (Shearer and Buehler, 2019), and Ps and Sp receiver functions (e.g. Bostock, 1998; Chen et al., 2009). Sp and Ps phases generated at negative velocity gradients have been observed on a widespread if intermittent basis, often at depths of 60-110 km. The evidence for negative MLDs within the cratonic lithosphere includes detections in North America, Australia, southern Africa, Tanzania, India, China, and Europe (e.g. Rychert and Shearer, 2009; Savage and Silver, 2008; Hansen et al., 2009; Miller and Eaton, 2010; Ford et al., 2010; Geissler et al., 2010; Wölbern et al., 2012; Kind et al., 2012; Bodin et al., 2013; Sodoudi et al., 2013; Foster et al., 2014b; Wirth and Long, 2014; Hopper and Fischer, 2015; Porritt et al., 2015; Hansen et al., 2015; Kind et al., 2017; Sun and Kennett, 2017; Hopper and Fischer, 2018; Kind and Yuan, 2019) although the existence of widespread MLDs in the U.S. has recently been challenged (Kind et al., 2020). While their long-wavelength nature precludes a detection of a sharp boundary, surface-wave phase velocities in cratonic areas also support the presence of a layer of reduced velocities in the depth range of 60-100 Km (Lekic and Romanowicz, 2011; Dalton et al., 2017; Eeken et al., 2018).

A variety of origins have been proposed for the apparent widespread negative MLDs. One hypothesis is that the negative velocity gradients reflect the top of a layer whose velocities have been reduced by the presence of volatile-rich minerals crystallized from partial melt and/or produced by metasomatism (Abt et al., 2010; Wölbern et al., 2012; Selway et al., 2015; Rader et al., 2015; Hansen et al., 2015; Hopper and Fischer, 2015; Aulbach et al., 2017; Saha et al., 2018; Eeken et al., 2018). Vertical variations in seismic anisotropy are another commonly invoked origin (e.g. Bostock, 1998; Yuan and Romanowicz, 2010; Sodoudi et al., 2013; Wirth and Long, 2014), and the effects of fine-scale laminar structure have also been proposed (e.g. Kennett et al., 2017; Sun and Kennett, 2017). Both metasomatic products and anisotropy may represent relict lithospheric structures produced by subduction (Bostock, 1998; Chen et al., 2009; Cooper and Miller, 2014; Hopper and Fischer, 2015; Cooper et al., 2017). Anelastic relaxation from grain boundary sliding is another proposed mechanism for the velocity reduction (e.g. Karato, 2012; Karato et al., 2015; Karato and Park, 2019). A downward decrease in melt depletion and Mg# has also been proposed as a contributing factor in creating negative MLDs, but many studies have concluded that velocity decreases due to reductions in Mg# alone would be too small to explain larger (>2%) observed MLD velocity changes (e.g. Selway et al., 2015; Karato et al., 2015). Discussions of the merits and weaknesses of other origin models can be found in recent review papers (e.g. Selway, 2019; Karato and Park, 2019). Layers of mechanically weak mantle associated with MLDs have been implicated in models for the destruction of cratonic lithosphere (e.g. Snyder et al., 2017; Liu et al., 2018; Hu et al., 2018).

Like the existence of MLDs, absolute shear velocity within the cratonic lithosphere is difficult to explain by temperature and pressure variations alone (Bruneton et al., 2004; Pedersen et al., 2009; Lebedev et al., 2009; Hieronymus and Goes, 2010; Hirsch et al., 2015; Dalton et al., 2017; Eeken et al., 2018; Garber et al., 2018). First, the depth dependence of cratonic V_S profiles is perplexing: in many models, V_S increases from the Moho to depths of ~100-150 km (Fig. 5). When such V_S profiles are mapped into temperature assuming a constant peridotite composition, the resulting temperature structures are found to conflict with geotherms estimated from mantle xenolith thermobarometry, surface heat flow, and seismic attenuation, and with the overall concept of a thick thermal boundary layer beneath cratons. Dalton et al. (2017) and Eeken et al. (2018) showed that the existence of a low-velocity layer in the uppermost mantle lithosphere (~90-km depth), potentially associated with MLDs, can help resolve the discrepancy between observations and predictions, although both studies concluded that an additional mechanism is needed in the 150-250 km depth range to produce high velocities. Second, cratonic V_S profiles are characterized by very high values (4.7-4.8 km/s) that are difficult to reconcile with predictions of realistic mantle geotherms and peridotite compositions, even when the coldest end-member geotherm and a highly depleted dunitic composition are used, leading some researchers to propose the presence of ~20% eclogite or ~2% diamond in cratonic lithosphere (Garber et al., 2018). Although few V_S models incorporate lithospheric discontinuities, the literature on joint inversions of phase velocities and converted phases shows that the acceptable seismic models change depending on which data sets are inverted (e.g. Eilon et al., 2018). It is possible that such joint inversions will reveal a common origin for MLDs and the perplexing aspects of depth-dependent V_S profiles.

4. Oceans vs. continents: do body wave discontinuities and surface wave data reflect the same lithospheric boundary layer?

A key issue when comparing oceanic and continental lithospheres is to determine whether scattered and reflected body wave phases and surface waves are consistent with the same lithospheric thickness, or whether the two data types require multiple velocity gradients. In relatively young, tectonically active continental regions, the estimates of lithospheric properties from the two data types are typically consistent. The relatively thin lithosphere with a vertically localized velocity gradient at its base often indicated by the converted/reflected body waves also matches surface wave phase velocities (e.g. Fig. 8). In contrast, in the ancient, cratonic continental lithosphere, mid-lithospheric discontinuities at depths of less than 120 km represent layering internal to the lithosphere, given that surface wave data in cratons require high velocity mantle to depths of 150 km or more (Section 3.4).

The answer for the oceanic lithosphere is less clear. As previously discussed, the converted/reflected phases typically indicate a boundary at 50-90 km depth for lithosphere of more than 50 Myr in age, with smaller discontinuity depths at younger ages (Fig. 4). These depths broadly correspond to the lower margin of the thermally-defined lithosphere for a cooling plate model where the asymptotic lithospheric thickness (the thickness at infinite age) is 50-90 km. These converted/reflected phase observations are consistent with some models that incorporate surface wave data, but not others. The converted/reflected phase depths are broadly consistent with the base of the high velocity lithosphere in the SEMum2 model (French et al., 2013). The depths of the minimum asthenospheric velocity in the SEMum2 model (orange x's in Fig. 4) can be considered a maximum value for lithospheric thickness, and these values overlap with many of the converted/reflected phase depths. However, other surface wave studies have produced divergent conclusions on even the basic question of whether a cooling plate model or a half-space cooling model better characterizes the oceanic lithosphere. Ritzwoller et al. (2004) argued that a plate model was needed to explain their Rayleigh wave inversion results, and Ma and Dalton (2019) concluded, using a forward-modeling approach, that a cooling plate model fits the dependence of Rayleigh wave phase velocity on seafloor age in much of the Pacific and Atlantic basins better than a half-space model. On the other hand, several other shear-wave velocity models constrained from inversions of Rayleigh wave velocities have favored a half-space cooling model (e.g. Maggi et al., 2006). With forward modeling, Beghein and Goes (2019) obtained distributions of V_{SV} models compatible with published Rayleigh wave phase velocity maps and compared those models with synthetic velocity models calculated with Perple_X (Connolly, 2009) for various plate and half-space cooling models. These models also accounted for anelastic effects using different attenuation models. The authors found that both the tomographic results and the half-space cooling synthetic models predict differences in velocities for different ages that persist down to depths of 175 km, which is significantly deeper than the plate cooling model predictions.

Here we present a new test of this question for the entire Pacific oceanic lithosphere. This test seeks to assess whether oceanic lithosphere that corresponds to a thermal boundary layer, whose thickness agrees with the depths of body wave conversion and reflection in the oceans (50-90 km) (Fig. 4), can also match surface wave phase

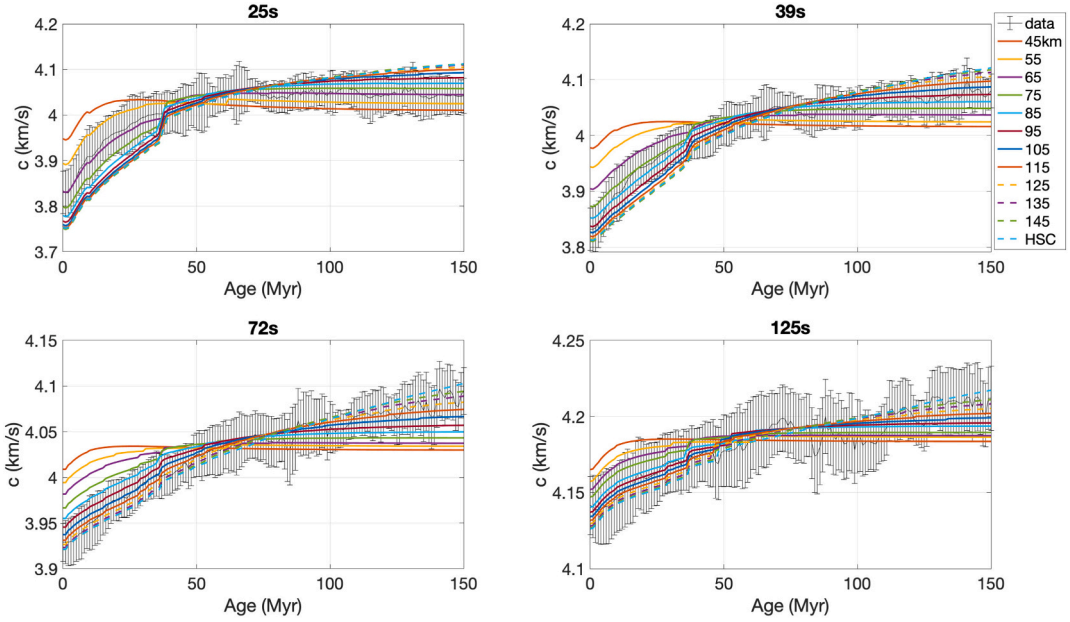

Fig. 10. Comparison of observed (error bars) and predicted (colored lines) phase velocities for the Pacific Ocean at four periods (25 s, 39 s, 72 s and 125 s). Observed phase velocities are sampled from the GDM52 phase velocity maps of Ekström (2011) in 11,586 1^{o}x1^{o} cells. Predictions are shifted to have the same median velocity over the age range 0-150 Myr to compare to the observations. Error bars show the median phase velocity, determined in a sliding 2-Myr-wide age bin, with height equal to twice the standard deviation. These predictions are based on plate cooling thermal models with a mantle potential temperature of 1350°C and a grain size of 10 mm for the anelastic calculation. Different colors correspond to different assumptions about the asymptotic plate thickness, including the end-member case of half-space cooling (HSC).

velocities. The test compared the predictions of cooling models to absolute Rayleigh wave phase velocities across the entire Pacific basin, spanning crustal ages of 0-150 Myr. Observed phase velocities included 34 periods between 25 s and 250 s from the global GDM52 phase velocity maps of Ekström (2011). Observed phase velocity was compared to predicted phase velocity at each period. By directly modeling phase velocities, rather than modeling shear velocities, we avoided complications introduced by assumptions about smoothing and parameterization in the conversion of phase velocities to depth-dependent shear velocity models.

Predicted phase velocities represent a range of mantle conditions. The plate cooling models used to represent temperature included values of asymptotic plate thickness that range from 45 to 145 km and values of mantle potential temperature that vary from 1350°C to 1450°C. The half-space cooling model was also tested for the same mantle potential temperatures. Assuming these thermal models and a harzburgite composition, Perple_X (Connolly, 2009) was used to predict elastic Vs, Vp, and density in the upper mantle using the thermodynamic parameters and solution model from Stixrude and Lithgow-Bertelloni (2011). The anelastic reduction of shear velocity given the assumed thermal structure was estimated from Jackson and Faul (2010), using grain size values of 1 mm and 10 mm, which yielded larger and smaller anelastic effects, respectively. For each age between 0 Myr and 150 Myr (1-Myr increments), we constructed depth-dependent models that first assumed the upper mantle structure described above for depths of 0 to 410 km, but then replaced the shallowest structure with a sediment layer (0.15 km) and a crustal layer (6.24 km) constrained by seismic data from the NoMelt array of ocean-bottom seismometers on 70-Myr Pacific seafloor (Russell et al., 2019; Ma et al., 2020). A water layer whose thickness depends on seafloor age (Stein and Stein, 1992) was emplaced on top of the sediments. The PREM velocity model (Dziewonski and Anderson, 1981) was assumed for the transition zone, lower mantle, and core.

For each 1-Myr increment, Rayleigh wave phase velocities were predicted using MINEOS (Masters et al., 2007). Although significant

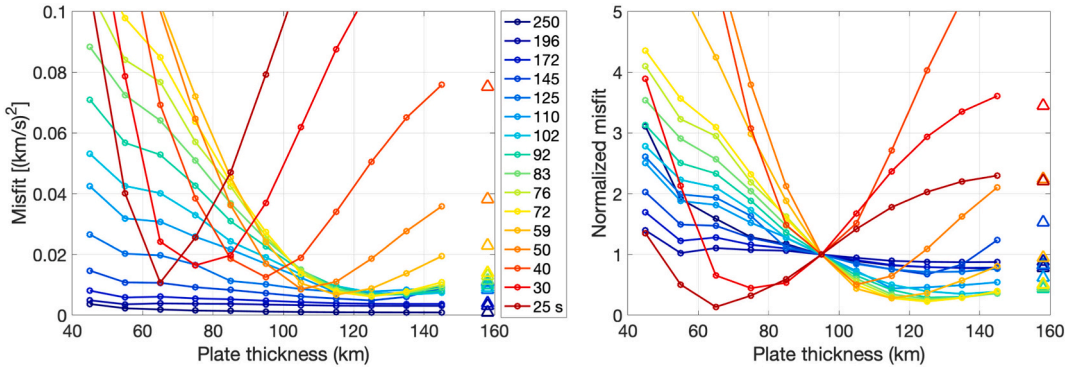

Fig. 11. Misfits between predicted and observed phase velocities, where the median observed velocity in a sliding 2-Myr-wide age bin is used. Misfit is defined as the sum over the age range 35-150 Myr of the squared difference for a given period (line color) and plate thickness (horizontal axis). (Left) Total misfit between predicted and observed phase velocities. (Right) As in (left) but here misfit at each period has been normalized by its value for a 95 km plate thickness. Triangles show misfit for half-space cooling models. All models assume a mantle potential temperature of 1350°C and a grain size of 10 mm.

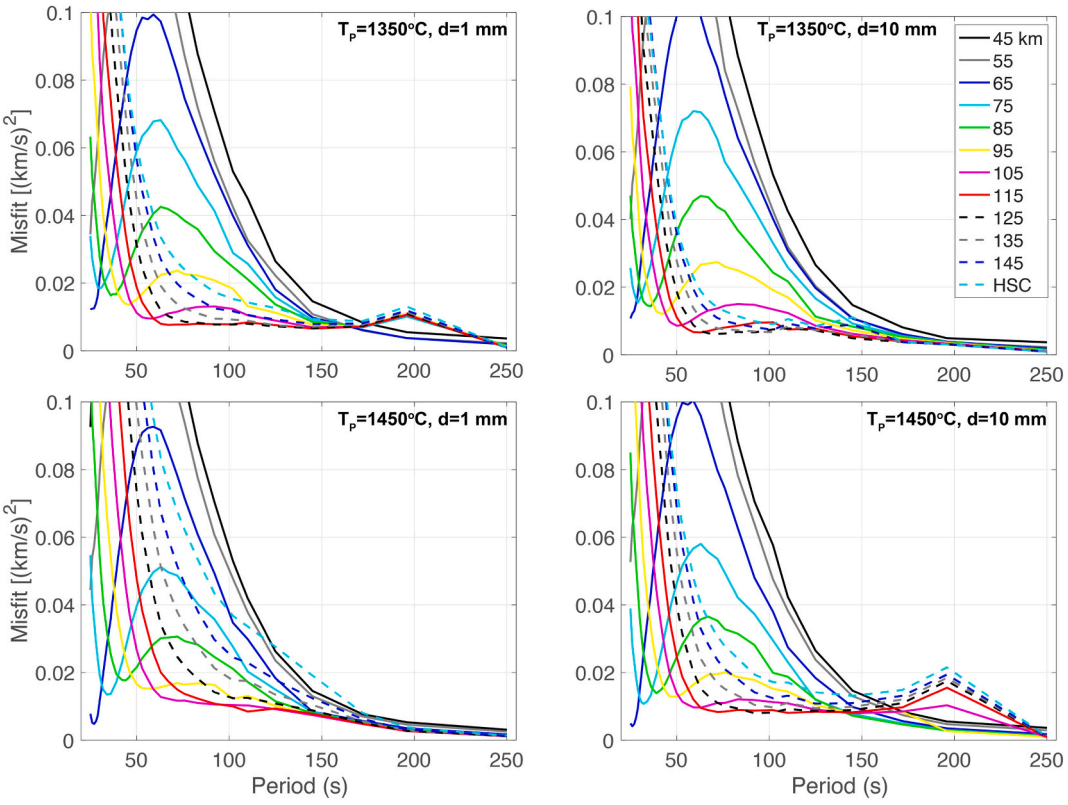

Fig. 12. Misfit versus period for models with: (upper) 1350°C and (lower) 1450°C mantle potential temperature with (left) 1 mm grain size and (right) 10 mm grain size. Different colors correspond to different assumptions about the asymptotic plate thickness, including half-space cooling (HSC). Misfit is calculated as in Fig. 11.

scatter exists in the phase velocities at a given crustal age for a given period (Fig. 10), the observations still have the ability to rule out certain plate thicknesses for periods of approximately 90 s or less. For example, at 39 s the increase in phase velocity with age predicted using a 45 km thick plate is much smaller than the observed increase, whereas with a 145 km thick plate the predicted increase is larger than observed. At longer periods (e.g. 125 s in Fig. 10) differences between the predictions of different plate thicknesses are smaller and many models fit the data reasonably well.

Misfits between observed and predicted phase velocities were quantified after normalizing the values so that at each period the observations and predictions have the same median phase velocity. With this normalization, the misfit depends largely on how well the age dependence of the predictions matches the age dependence of the observations. In general the size of the normalization correction is less than 0.05 km/s, although it is slightly larger for the thinnest plates (45-55 km) at the shortest periods (<44 s). Misfits were obtained by summing the squares of the differences between observed and predicted phase velocities; the median observed velocity in a sliding 2-Myr age bin was used. Misfit is shown in Fig. 11 as total misfit (left) and normalized by its value for a 95 km plate thickness (right) so that variations within and between periods are easier to discern. In these examples, the models assume a mantle potential temperature of 1350°C and a grain size of 10 mm.

The misfit values reveal several clear results. First, sensitivity to plate thickness increases as period decreases. The shortest periods (red and orange, Fig. 11) show both greater variations in misfit and better-defined minima than the longest periods (blue). Second, the best-fitting plate thickness increases from the shortest periods (periods of 25 s to 32 s) to intermediate periods (35 s to 90 s) while periods of 120 s and higher are comparably well fit by a wide range of plate thicknesses. These trends are also evident in plots of misfit as a function of period (Fig. 12) for the 1350°C asthenospheric temperature and 10 mm grain size models. Fig. 12 also demonstrates that these results do not strongly depend on assumptions about mantle potential temperature and grain size.

Best-fitting asymptotic plate thicknesses as a function of period are shown in Fig. 13. Uncertainties in the best-fitting asymptotic plate thicknesses for each period were estimated as the range of thermal models, including the half-space cooling model, whose predictions fall within one standard deviation of the median phase velocity for 90% of the ages under consideration. For the models with 1350°C asthenospheric temperature and 10 mm grain size, a plate thickness of 95 km overlaps the uncertainties of the best-fit model at all periods. For the other sets of models, a plate thickness of 95 km overlaps the confidence limits at periods of more than 35 s, whereas at the shortest periods (<35 s), the data for some cases require plate thicknesses of 85 km. Results for ages limited to 0-70 Myr-old lithosphere are very similar. The variation in the minimum-misfit model as a function of period, with the shortest periods preferring a 65 km plate thickness and periods near 75 s period preferring a plate thickness of 105-125 km (Fig. 13), is an interesting topic for future inquiry. The temperature dependence of attenuation and its impact on shear velocity vary between attenuation models (e.g. Goes et al., 2012; Abers et al., 2014), and different anelastic effects might reduce the period-dependence of best-fitting plate thicknesses.

The range of asymptotic plate thicknesses (85-95 km) indicated by the Rayleigh wave phase velocities are consistent with heat flow data (Hasterok, 2013b), and they produce oceanic thermal boundary layers whose thicknesses as a function of age broadly match the depth distribution of the converted/reflected phase observations. For a cooling plate with an asymptotic thickness of 95 km and a mantle potential temperature of 1350°C, the 900°C to 1300°C plate model isotherms span much of the depth range of converted/reflected phases (black lines in comparison to symbols in Fig. 4). This is generally expected because the maximum negative velocity gradient produced by a cooling plate model lies above the depth of its deepest isotherm (Fig. 3a). Greater depth

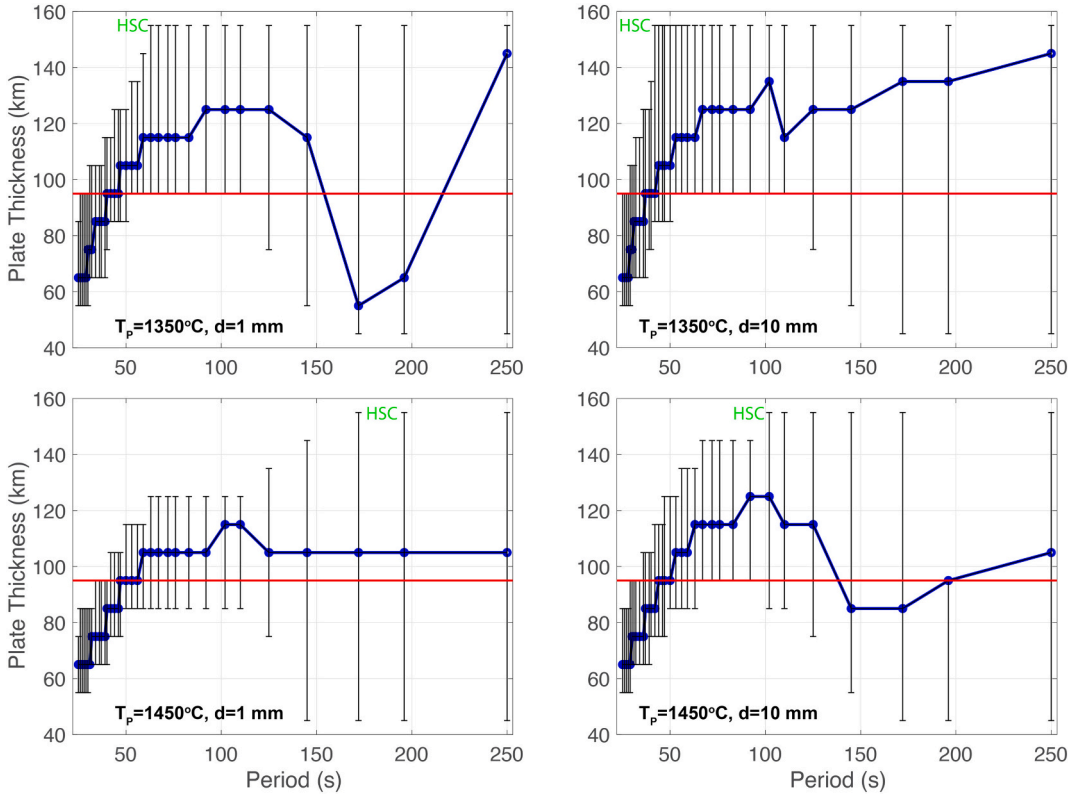

Fig. 13. Best-fitting asymptotic plate thickness as a function of Rayleigh wave period for 35-150 Myr-old lithosphere. Results are shown for thermal models with: (upper) 1350°C and (lower) 1450°C mantle potential temperature with (left) 1 mm grain size and (right) 10 mm grain size. Blue curve shows plate thickness corresponding to the minimum misfit at each period. Error bars show the range of plate thickness for which predicted phase velocity falls within one standard deviation of the observed median value (e.g., Fig. 11). For plotting purposes only, results for half-space cooling (HSC) are shown as plate thickness = 155 km. In all cases, plate thicknesses of 85-95 km overlap the confidence limits. Results for ages limited to 0-70 Myr-old lithosphere are very similar.

variability in the converted/reflected wave results in comparison to the narrower, 85-95 km, preferred plate thickness range from the Pacific-wide averaged Rayleigh waves could be due to the higher sensitivity of the individual scattered wave results to lateral variability in mantle structure (e.g. Fig. 2b). Accounting for these factors, the Rayleigh wave phase velocities and the converted/reflected wave discontinuity depths are both broadly consistent with lithospheric thicknesses that increase as a function of seafloor age to the same range of maximum values.

Having established the overall consistency between the depths of oceanic converted/reflected wave discontinuities and the range of asymptotic plate thicknesses from Rayleigh phase velocities, the next question is whether the LAB velocity gradients predicted for these simple cooling models are sufficient to produce observable converted and reflected phases. To address this question, at least in part, we calculated synthetic Sp receiver functions for the shear velocity models predicted by asymptotic plate thicknesses of 65 km and 95 km, seafloor ages of 20 Ma, 40 Ma, and 80 Ma, a mantle potential temperature of 1350°C, and a 10 mm grain size (Fig. 14). Sediment and water layers in the shear velocity models were replaced with oceanic crust, to simplify predicted crustal phases. For the receiver functions, we assumed a dominant period of 8 s for the incident S phase, a bandpass filter from 100 s to 2 s (which is in the range of commonly used values), a typical ray parameter of 0.11 km/s, and time domain deconvolution (Ligorria and Ammon, 1999) with a Gaussian shaping function whose half-width is 0.8 s. In Fig. 14, Sp phase polarities have been reversed to agree with the Ps convention, where positive phases correspond to velocity increases with depth, and negative phases show velocity decreases with depth.

While the synthetic Sp receiver functions contain large positive phases from the Moho, the amplitudes of the negative phases generated by the LAB velocity gradients are highly variable. At young lithospheric ages, represented in Fig. 14 by 20 Myr, the velocity contrast between lithosphere and asthenosphere is small, and the LAB velocity gradient generates only a small negative Sp phase that would be difficult to observe with signal-to-noise ratios typical of real data. At 40 Myr, the cooler lithosphere has higher velocities that create a greater velocity contrast with the asthenosphere. This velocity gradient in turn generates larger amplitude negative Sp phases that would be challenging, but possible, to observe in real data. At 80 Myr, the model for the 65 km asymptotic plate thickness has a LAB velocity gradient that produces a clear phase with an observable amplitude, but in the model for the 95 km plate, the LAB velocity gradient is too gradual and the LAB phase is low amplitude and distributed over a wide depth range. Overall, while these thermally-controlled velocity gradients have some potential to generate observable Sp phases at ages of 40-80 Myr, they fail for both young oceanic lithosphere and older lithosphere with the 95 km plate thickness that is most consistent with the Rayleigh wave phase velocities. The fact that the depths of the predicted LAB phases are shallower than the asymptotic plate thickness is another illustration that the maximum negative shear velocity gradient lies within the cooling boundary layer, thus explaining the depth offset between the majority of the scattered and reflected phase depths and the deepest isotherms for the 95 km plate model (Fig. 4).

To explain converted phase arrivals at the full span of oceanic lithospheric ages where they are observed (Fig. 4), an additional factor must reduce asthenospheric velocities and create larger LAB velocity gradients. The presence of a small amount of partial melt in the oceanic asthenosphere could easily produce the necessary velocity reduction (e.g. Chantel et al., 2016). Partial melt could be present on a widespread basis beneath the oceanic lithosphere if 500 ppm of water was present in the asthenosphere, and if the melt collected below the solidus at the

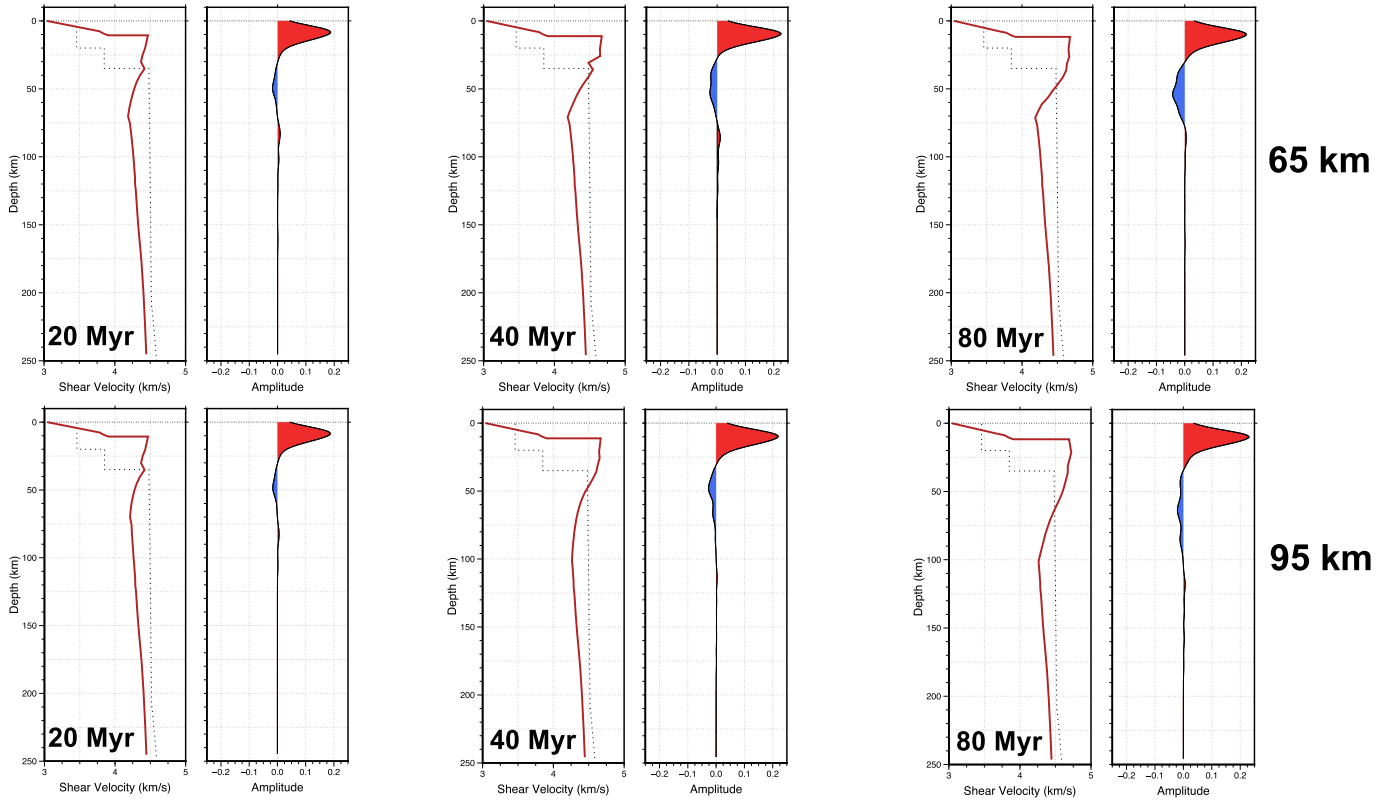

Fig. 14. In each pair, plots show shear velocity models predicted by asymptotic plate thicknesses of 65 km and 95 km, seafloor ages of 20 Myr, 40 Myr, and 80 Myr, an asthenospheric temperature of 1350°C, and a 10 mm grain size. Dotted lines show the AK135 reference model (Kennett et al., 1995). Plots on right show Sp receiver functions assuming a dominant period of 8 s, a bandpass filter from 100 s to 2 s, and time domain deconvolution (Ligorria and Ammon, 1999) with a 0.8 s Gaussian. The polarity of the Sp phases has been reversed to agree with the Ps convention, where positive phases correspond to velocity increases with depth, and negative phases show velocity decreases with depth. The large red (positive) phase corresponds to the oceanic Moho, and the blue (negative) arrival beneath it is from the LAB velocity gradient. The effects of sediment and water layers are ignored by replacing them with basement velocities. Depth in these plots is measured from the sea surface. LAB phases for 40 Myr and for the 65 km plate model at 80 Myr are large enough to be potentially observable. LAB amplitudes for other conditions are too small and would likely be swamped by noise in real data.

upper boundary of the partial melt layer beneath a 95 km thick plate (shallower pink line, Fig. 4) the LAB velocity gradient could be increased enough to produce higher amplitude, easily observable phases. Alternatively, melting of carbonated oceanic asthenospheric mantle could also enhance the LAB velocity gradient, in which case volatile contents typical of the mantle sources of mid-ocean ridge basalts (100 ppm H_2O, 60 ppm CO_2) can produce partial melt even beneath the oldest oceanic lithosphere (Hirschmann, 2010). While a thermal boundary enhanced by the presence of partial melt is a viable explanation, contributions to the LAB velocity gradient from other mechanisms, including elastically accommodated grain boundary sliding (Karato, 2012; Olugboji et al., 2013) and velocity anisotropy, are also possible (see Section 2.2).

For young continents, while the depths of LAB velocity gradients implied by scattered and reflected phases are often compatible with the thickness of high velocity lithosphere observed with surface waves (Fig. 8, references in Section 3), the need for partial melt below this boundary is harder to assess. The magnitudes of purely thermal LAB velocity gradients obviously depend on assumed thermal structure, which for the more complex tectonic histories within the continents is much less well-constrained than for the oceanic lithosphere. Steady-state conductive geotherms that match continental heat flow typically produce gradual velocity gradients that are not capable of matching converted and reflected body wave LAB arrivals (e.g. Cammarano and Guerri, 2017). For example, when the steady-state thermal models of Cammarano and Guerri (2017) for the western U.S. are converted to shear velocity using the scaling relationships of Jackson and Faul (2010), a 1-10 mm grain size, and a dominant period of 10 s, the resulting magnitudes of the shear velocity drop across the LAB gradient are large (up to 8%), but they are distributed over depths of 60-70 km (Hopper and Fischer, 2018). These velocity gradients are comparable in depth range, but slightly smaller in magnitude, relative to the LAB velocity gradient for 80 Myr oceanic lithosphere with a 95 km asymptotic plate thickness (Fig. 14), although absolute velocities would differ significantly. Thus steady-state continental geotherms fail to predict significant and observable Sp phases. However, if asthenospheric upwelling or removal of the lower lithosphere results in isotherms that are concentrated in a smaller depth range, and if temperature contrasts between lithosphere and asthenosphere are sufficiently large, purely thermal models could produce Sp phases with amplitudes comparable to those observed in regions such as the Phanerozoic U.S. (e.g. Fig. 8; Hansen et al., 2015; Hopper and Fischer, 2018, Eilon et al., 2018) or Phanerozoic Europe (e.g. Geissler et al., 2010). Nonetheless, the physical viability of such strong vertical temperature gradients is unclear. For example, purely thermal models would require ubiquitous strong upwelling or convective removal of the lower thermal boundary layer beneath the broad regions of the western U.S. that contain large Sp arrivals and strong LAB velocity gradients (Hansen et al., 2015; Hopper and Fischer, 2018). Therefore, the presence of small fractions of partial melt at the base of the thermal lithosphere appears to be a more straightforward explanation.

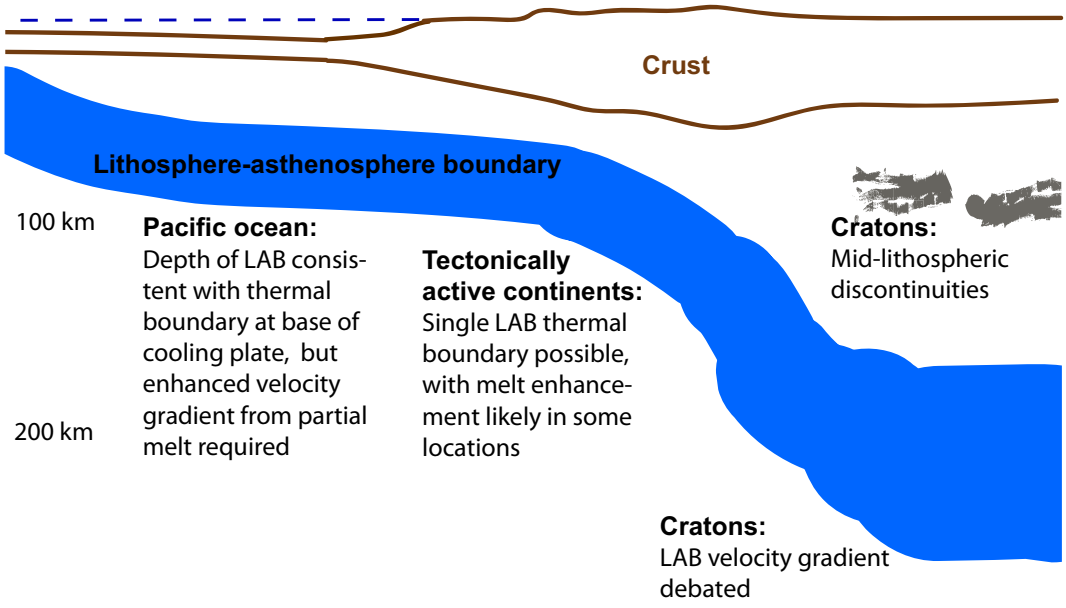

Fig. 15. Schematic figure showing interpretation of LAB properties that are consistent with constraints from Rayleigh waves and converted and reflected body wave phases.

5. Conclusions: a synoptic view of the LAB across oceans and continents

This review of LAB properties beneath oceans and continents, coupled with the new modeling of Rayleigh wave phase velocities in the Pacific ocean and the amplitudes of Sp converted phases, provides the basis for an overview of isotropic LAB structure globally. In many respects, the oceanic lithosphere and relatively young (non-cratonic) continental lithosphere share similarities, whereas the properties of the cratonic LAB are less certain.

Beneath the oceans, surface wave constraints on lithospheric thickness are compatible with the depths of LAB velocity gradients implied by converted and scattered body wave observations (Fig. 15). However, in the case of Pacific oceanic lithosphere, the LAB velocity gradients for the asymptotic plate thicknesses (85-95 km) that are consistent with both Rayleigh wave and heat flow (Hasterok, 2013b) produce Sp phases that are too small to be observable, both at ages less than 30 Ma and at ages of 80 Ma or more. Sp phases and other scattered and reflected body waves that are observed at these ages (Fig. 4) could be explained by partial melt, from hydrated and/or carbonated asthenosphere, that has collected below its solidus and enhanced the LAB velocity gradient. Vertically localized and/or laminated melt layers are also a possible explanation for even sharper velocity gradients observed with scattered waves (e.g. Kawakatsu et al., 2009) and active source data (Stern et al., 2015; Mehouachi and Singh, 2018).

Beneath young continental lithosphere, surface wave constraints on lithospheric thickness are also compatible with the depths of LAB velocity gradients implied by converted and scattered body wave observations (Fig. 15). Due to the greater complexity in their tectonic histories, it is harder to assess whether temperature alone can explain the magnitudes of LAB velocities gradients in these regions. However, unless strong upwelling or convective removal of the lower thermal boundary layer is assumed, the presence of an additional factor, such as partial melt at the base of the thermal lithosphere, is needed to sharpen LAB velocity gradients.

In cratonic continental regions, the thickness of the high velocity mantle lithosphere indicated by surface waves is significantly greater than the depths where body wave conversions and reflections are most commonly observed, providing evidence for velocity layering internal to the cratonic mantle, although such layering appears to be laterally discontinuous (Fig. 15). Debate continues regarding cratonic LAB velocity gradients, with some studies concluding that they are gradual in depth and consistent with steady-state thermal models, and other studies inferring more vertically localized velocity gradients that involve additional physical or chemical factors.

Declaration of Competing Interest

The authors declare that they have no known competing financial interests or personal relationships that could have appeared to influence the work reported in this paper.

Acknowledgements

Our thanks to CIDER (Cooperative Institute for Dynamic Earth Research) for funding the workshop that initiated this paper, and to the editor and two reviewers for their helpful feedback. Work on this paper was supported by NSF awards EAR-1829401 (K.M.F.), EAR-1553367 (C. A.D.), EAR-1925595 (D.L.S), NERC awards NE/M003507/1/339 and NE/K010654/1, and ERC award GA 638665 (C.A.R).

References

Abers, G.A., Fischer, K.M., Hirth, G., Wiens, D.A., Plank, T., Holtzman, B.K., McCarthy, C., Gazel, E., 2014. Reconciling mantle attenuation-temperature relationships from seismology, petrology, and laboratory measurements (2014, Sep). Geochemistry Geophysics Geosystems 15 (9), 3521–3542. https://doi.org/10.1002/2014gc005444.

Abt, D.L., Fischer, K.M., French, S.W., Ford, H.A., Yuan, H., Romanowicz, B., 2010. North American lithospheric discontinuity structure imaged by Ps and Sp receiver functions. J. Geophys. Res. 115 (B09301), 1–24. https://doi.org/10.1029/2009JB006914.

Adams, A., Nyblade, A., Weeraratne, D., 2012. Upper mantle shear wave velocity structure beneath the East African plateau: evidence for a deep, plateau-wide low velocity anomaly. Geophys. J. Int. 189, 123–142. https://doi.org/10.1111/j.1365-246X.2012.05373.x.

Afonso, J.C., Schutt, D.L., 2012. The effects of polybaric partial melting on density and seismic velocities of mantle restites. Lithos 134–135, 289–303.

Afonso, J.C., Ranalli, G., Fernàndez, M., Griffin, W.L., O'Reilly, S.Y., Faul, U., 2010. On the Vp/Vs–Mg# correlation in mantle peridotites: Implications for the identification of thermal and compositional anomalies in the upper mantle. Earth Planet. Sci. Lett. 289, 606–618.

Audet, P., 2016. Receiver functions using OBS data: Promises and limitations from numerical modelling and examples from the Cascadia Initiative. Geophys. J. Int. 205, 1740–1755. https://doi.org/10.1093/gji/ggw111.

Auer, L., Boschi, L., Becker, T.W., Nissen-Meyer, T., Giardini, D., 2014. Savani: a variable resolution whole-mantle model of anisotropic shear-velocity variations based on multiple datasets. J. Geophys. Res. 119, 3006–3034. https://doi.org/10.1002/2013JB010773.

Auer, L., Becker, T., Boschi, L., Schmerr, N., 2015. Thermal structure, radial anisotropy, and dynamics of oceanic boundary layers. Geophys. Res. Lett. 42, 9740–9749. https://doi.org/10.1002/2015gl066246.

Aulbach, S., Massuyeau, M., Gaillard, F., 2017. Origins of cratonic mantle discontinuities: a view from petrology, geochemistry and thermodynamic models. Lithos 68, 364–382.

Bagley, B., Revenaugh, J., 2008. Upper mantle seismic shear discontinuities of the Pacific. J. Geophys. Res. 113 (B12).

Becker, T.W., 2017. Superweak asthenosphere in light of upper mantle seismic anisotropy. Geochem. Geophys. Geosyst. 18, 1986–2003. https://doi.org/10.1002/2017GC006886.

Beghein, C., Yuan, K.Q., Schmerr, N., Xing, Z., 2014. Changes in seismic anisotropy shed light on the nature of the Gutenberg Discontinuity. Science 343, 1237–1240. https://doi.org/10.1126/science.1246724.

Beghein, C., Xing, Z., Goes, S., 2019. Thermal nature and resolution of the lithosphere-asthenosphere boundary under the Pacific from surface waves. Geophys. J. Int. 216, 1441–1465. https://doi.org/10.1093/gji/ggy490.

Behn, M.D., Hirth, G., Elsenbeck, J.R., 2009. Implications of grain size evolution on the seismic structure of the oceanic upper mantle. Earth Planet. Sci. Lett. 282, 178–189. https://doi.org/10.1016/J.Epsl.2009.03.014.

Bodin, T., Yuan, H., Romanowicz, B., 2013. Inversion of receiver functions without deconvolution - application to the Indian craton. Geophys. J. Int. 196, 1025–1033. https://doi.org/10.1093/gji/ggt431.

Bostock, M.G., 1998. Mantle stratigraphy and evolution of the Slave Province. J. Geophys. Res. 103, 21,183–121,200.

Boyd, F.R., 1989. Compositional distinction between oceanic and cratonic lithosphere. Earth Planet. Sci. Lett. 96, 15–26.

Bruneton, M., Pedersen, H.A., Vacher, P., Kukkonen, I.T., Arndt, N.T., Funke, S., Friederich, W., Farra, V., 2004. Layered lithospheric mantle in the central Baltic shield from surface waves and xenolith analysis. Earth Planet. Sci. Lett. 226, 41–52. https://doi.org/10.1016/j.epsl.2004.07.034.

Burgos, G., Montagner, J.-P., Beucler, E., Capdeville, Y., Mocquet, A., Drilleau, M., 2014. Oceanic lithosphere–asthenosphere boundary from surface wave dispersion data. J. Geophys. Res. 119, 1079–1093. https://doi.org/10.1002/2013jb010528.

Calo, M., Bodin, T., Romanowicz, B., 2016. Layered structure in the upper mantle across North America from joint inversion of long and short period seismic data. Earth Planet. Sci. Lett. 449, 164–175. https://doi.org/10.1016/j.epsl.2016.05.054.

Cammarano, F., Guerri, M., 2017. Global thermal models of the lithosphere. Geophys. J. Int. 210, 56–72. https://doi.org/10.1093/gji/ggx144.

Chantel, J., Manthilake, G., Andrault, D., Novella, D., Yu, T., Wang, Y., 2016. Experimental evidence supports mantle partial melting in the asthenosphere. Sci. Adv. 2, e1600246.

Chen, C.W., Rondenay, S., Evans, R.L., Snyder, D.B., 2009. Geophysical detection of relict metasomatism from an Archean (~3.5 Ga) subduction zone. Science 326, 1089–1091.

Chen, L., Jiang, M., Yang, J., Wei, Z., Liu, C., Ling, Y., 2014. Presence of an intralithospheric discontinuity in the central and western North China Craton: Implications for destruction of the craton. Geology 42, 223–226. https://doi.org/10.1130/G35010.1.

Chu, R., Schmandt, B., Helmberger, D.V., 2012. Upper mantle P velocity structure beneath the Midwestern United States derived from triplicated waveforms. Geochem., Geophys., Geosys. 13, Q0AK04 https://doi.org/10.1029/2011GC003818.

Clark, A.N., Lesher, C.E., 2017. Elastic properties of silicate melts: implications for low velocity zones at the lithosphere-asthenosphere boundary. Sci. Adv. 3.

Clerc, F., Behn, M.D., Parmentier, E.M., Hirth, G., 2018. Predicting rates and distribution of carbonate melting in oceanic upper mantle: implications for seismic structure and global carbon cycling. Geophys. Res. Lett. 45, 6944–6953. https://doi.org/10.1029/2018GL078142.

Connolly, J.A.D., 2009. The geodynamic equation of state: what and how. Geochem. Geophys. Geosys. 10 https://doi.org/10.1029/2009GC002540. Q10014.

Cooper, C.M., Miller, M.S., 2014. Craton formation: internal structure inherited from closing of the early oceans. Lithosphere 6, 35–42.

Cooper, C.M., Miller, M.S., Moresi, L.M., 2017. The structural evolution of the deep continental lithosphere. Tectonophysics 695, 100–121.

Crosby, A.G., McKenzie, D., 2009. An analysis of young ocean depth, gravity and global residual topography. Geophys. J. Int. 178, 1198–1219. https://doi.org/10.1111/j.1365-246X.2009.04224.x.

Crough, S., 1983. Hotspot Swells. Ann. Rev. Earth Planet. Sci. 11, 165–193.

Dalton, C.A., Bao, X., Ma, Z., 2017. The thermal structure of cratonic lithosphere from global Rayleigh wave attenuation. Earth Planet. Sci. Lett. 457, 250–262.

Debayle, E., Kennett, B.L.N., 2000. Anisotropy in the Australasian upper mantle from Love and Rayleigh waveform inversion. Earth Planet. Sci. Lett. 184, 339–351.

Debayle, E., Ricard, Y., 2012. A global shear velocity model of the upper mantle from fundamental and higher Rayleigh mode measurements. J. Geophys. Res. 117, 1–24.

Doin, M.P., Fleitout, L., 1996. Thermal evolution of the oceanic lithosphere: an alternative view. Earth Planet. Sci. Lett. 142, 121–136. https://doi.org/10.1016/0012-821x(96)00082-9.

Dziewonski, A.M., Anderson, D.L., 1981. Preliminary reference Earth model. Phys. Earth Planet. Int. 25, 297–356.

Eaton, D.W., Darbyshire, F., Evans, R.L., Grutter, H., Jones, A.G., Yuan, X., 2009. The elusive lithosphere–asthenosphere boundary (LAB) beneath cratons. Lithos 109, 1–22.

Eeken, T., Goes, S., Pedersen, H.A., Arndt, N.T., Bouilhol, P., 2018. Seismic evidence for depth-dependent metasomatism in cratons, Earth Planet. Sci. Lett. 491, 148–159.

Eilon, Z., Fischer, K.M., Dalton, C.A., 2018. An adaptive Bayesian inversion for upper-mantle structure using surface waves and scattered body waves. Geophys. J. Int. 214, 232–253.

Ekström, G., 2011. A global model of Love and Rayleigh surface wave dispersion and anisotropy, 25-250 s. Geophys. J. Int. 187, 1668–1686.

Fischer, K.M., 2015. Crust and lithospheric structure - seismological constraints on the lithosphere-asthenosphere boundary. In: Schubert, Gerald (Ed.), Treatise on Geophysics, 2nd edition. Elsevier, Oxford. https://doi.org/10.1016/B978-0-444-53802-4.00026-9. 587-612.

Fischer, K.M., Ford, H.A., Abt, D.L., Rychert, C.A., 2010. The lithosphere-asthenosphere boundary. Ann. Rev. Earth Planet. Sci. 38, 551–575. https://doi.org/10.1146/annurev-earth-040809-152438.

Ford, H.A., Fischer, K.M., Abt, D.L., Rychert, C.A., Elkins-Tanton, L.T., 2010. The lithosphere-asthenosphere boundary and cratonic lithospheric layering beneath Australia from Sp wave imaging. Earth Planet. Sci Lett. 300, 299–310. https://doi.org/10.1016/j.epsl.2010.10.007.

Ford, H.S., Fischer, K.M., Lekic, V., 2014. Localized shear in the deep lithosphere beneath the San Andreas fault system. Geology 42, 295–298. https://doi.org/10.1130/G35128.1.

Ford, H.A., Long, M.D., Wirth, E.A., 2016. Mid-lithospheric discontinuities and complex anisotropic layering in the mantle lithosphere beneath the Wyoming and Superior Provinces. J. Geophys. Res. 121, 6675–6697.

Foster, A., Nettles, M., Ekström, G., 2014a. Overtone interference in array-based Love-wave phase measurements. Bull. Seism. Soc. Am. 104, 2266–2277.

Foster, K., Dueker, K., Schmandt, B., Yuan, H., 2014b. A sharp cratonic lithosphere-asthenosphere boundary beneath the American Midwest and its relation to mantle flow. Earth Planet. Sci. Lett. 402, 82–89. https://doi.org/10.1016/j.epsl.2013.11.018.

French, S.W., Romanowicz, B.A., 2014. Whole-mantle radially anisotropic shear velocity structure from spectral-element waveform tomography. Geophys. J. Int. 199, 1303–1327. https://doi.org/10.1093/gji/ggu334.

French, S.W., Lekic, V., Romanowicz, B., 2013. Waveform tomography reveals channeled flow at the base of the oceanic asthenosphere. Science 342 (6155), 227–230. https://doi.org/10.1126/science.1241514.

Furumura, T., Kennett, B.L.N., 2005. Subduction zone guided waves and the heterogeneity structure of the subducted plate: intensity anomalies in northern Japan. J. Geophys. Res. 110.

Gaherty, J.B., Jordan, T.H., Gee, L.S., 1996. Seismic structure of the upper mantle in a central Pacific corridor. J. Geophys. Res. 101, 22291–22309.

Garber, J.M., Maurya, S., Hernandez, J.-A., Duncan, M.S., Zeng, L., Zhang, H.L., Faul, U., McCammon, C., Montagner, J.-P., Moresi, L., Romanowicz, B.A., Rudnick, R.L., Stixrude, L., 2018. Multidisciplinary constraints on the abundance of diamond and eclogite in the cratonic lithosphere. Geochem. Geophys. Geosys. 19, 2062–2086.

Geissler, W.H., Sodoudi, F., Kind, R., 2010. Thickness of the central and eastern European lithosphere as seen by S receiver functions. Geophys. J. Int. 181, 604–634. https://doi.org/10.1111/j.1365-246X.2010.04548.x.

Godfrey, K.E., Dalton, C.A., Ritsema, J., 2017. Seafloor age dependence of Rayleigh wave phase velocities in the Indian Ocean. Geochem. Geophys. Geosys. 18, 1926–1942. https://doi.org/10.1002/2017GC006824.

Goes, S., Armitage, J., Harmon, N., Smith, H., Huismans, R., 2012. Low seismic velocities below mid-ocean ridges: attenuation versus melt retention. J. Geophys. Res. 117.

Griffin, W.L., O'Reilly, S.Y., Ryan, C.G., 1999. The composition and origin of subcontinental lithospheric mantle. Geochem. Soc. Spec. Publ. 6, 13–45.

Gripp, A.E., Gordon, R.G., 2002. Young tracks of hotspots and current plate velocities. Geophys. J. Int. 150, 321–361.

Gung, Y., Panning, M., Romanowicz, B., 2003. Global anisotropy and the thickness of continents. Nature 422, 707–710.

Hacker, B.R., Abers, G.A., Peacock, S.M., 2003. Subduction factory 1. Theoretical mineralogy, densities, seismic wave speeds, and H_2O contents. J. Geophys. Res. 108.

Hammond, W.C., Humphreys, E.D., 2000. Upper mantle seismic wave velocity: effects of realistic partial melt geometries. J. Geophys. Res. 105, 10975–10986.

Hannemann, K., Kruger, F., Dahm, T., Lange, D., 2017. Structure of the oceanic lithosphere and upper mantle north of the Gloria Fault in the eastern mid-Atlantic by receiver function analysis. J. Geophys. Res. 122, 7927–7950. https://doi.org/10.1002/2016jb013582.

Hansen, S.E., Nyblade, A.A., Julia, J., 2009. Estimates of crustal and lithospheric thickness in sub-saharan Africa from S-wave receiver functions, South African. J. Geol. 112, 229–240. https://doi.org/10.2113/gssajg.112.3-4.229.

Hansen, S.M., Dueker, K.G., Stachnik, J.C., Aster, R.C., Karlstrom, K.E., 2013. A rootless rockies: support and lithospheric structure of the Colorado Rocky Mountains inferred from CREST and TA seismic data. Geochem. Geophys. Geosys. 14, 2670–2695. https://doi.org/10.1002/ggge.20143.

Hansen, S.M., Dueker, K., Schmandt, B., 2015. Thermal classification of lithospheric discontinuities beneath USArray. Earth Planet. Sci. Lett. 431 https://doi.org/10.1016/j.epsl.2015.09.009.

Harmon, N., Forsyth, D.W., Weeraratne, D.S., 2009. Thickening of young Pacific lithosphere from high-resolution Rayleigh wave tomography: a test of the conductive cooling model. Earth Planet. Sci. Lett. 278, 96–106.

Harmon, N., Rychert, C.A., Kendall, J.M., Agius, M., Bogiatzis, P., Tharimena, S., 2020. Evolution of the oceanic Lithosphere in the equatorial Atlantic from Rayleigh Wave tomography, evidence for small-scale convection from the PI-LAB experiment. Geochem. Geophys. Geosys. https://doi.org/10.1029/2020GC009174.

Hasterok, D., 2013a. Global patterns and vigor of ventilated hydrothermal circulation through young seafloor. Earth Planet. Sci. Lett. 380, 12–20. https://doi.org/10.1016/j.epsl.2013.08.016.
Hasterok, D., 2013b. A heat flow based cooling model for tectonic plates. Earth Planet. Sci. Lett. 361, 34–43.
Heit, B., Sodoudi, F., Yuan, X., Bianchi, M., Kind, R., 2007. An S receiver function analysis of the lithospheric structure in South America. Geophys. Res. Lett. 34.
Hieronymus, C.F., Goes, S., 2010. Complex cratonic seismic structure from thermal models of the lithosphere: effects of variations in deep radiogenic heating. Geophys. J. Int. 180, 999–1012 (doi:10.111/j.1365-246X.2009.04478.x).
Hirsch, A.C., Dalton, C.A., Ritsema, J., 2015. Constraints on shear velocity in the cratonic upper mantle from Rayleigh wave phase velocity. Geochem. Geophys. Geosys. 16 https://doi.org/10.1002/2015GC006066.
Hirschmann, M.M., 2010. Partial melt in the oceanic low velocity zone. Phys. Earth Planet. Int. 179, 60–71.
Hirth, G., Kohlstedt, D.L., 1995. Experimental constraints on the dynamics of the partially molten upper-mantle. 2. Deformation in the dislocation creep regime. J. Geophys. Res. 100, 15441–15449.
Hirth, G., Kohlstedt, D.L., 1996. Water in the oceanic upper mantle: implications for rheology, melt extraction and the evolution of the lithosphere. Earth Planet. Sci. Lett. 144, 93–108.
Hopper, E., Fischer, K.M., 2015. The meaning of mid-lithospheric discontinuities: a case study in the northern U.S. craton. Geochem. Geophys. Geosyst. 16, 4057–4083. https://doi.org/10.1002/2015GC006030.
Hopper, E., Fischer, K.M., 2018. The changing face of the lithosphere-asthenosphere boundary: Imaging continental scale patterns in upper mantle structure across the contiguous US with Sp converted waves. Geochem. Geophys. Geosyst. 19, 2593–2614.
Hopper, E., Ford, H.A., Fischer, K.M., Lekic, V., Fouch, M.J., 2014. The lithosphere-asthenosphere boundary and the tectonic and magmatic history of the northwestern United States. Earth. Planet. Sci. Lett. 402, 69–81. https://doi.org/10.1016/j.epsl.2013.12.016.
Hu, J., Liu, L., Faccenda, M., Zhou, Q., Fischer, K.M., Marshak, S., Lundstrom, C., 2018. Modification of the Western Gondwana craton by plume–lithosphere interaction. Nat. Geosci. 11, 203–210.
Hua, J., Fischer, K.M., Savage, M.K., 2018. The lithosphere–asthenosphere boundary beneath the South Island of New Zealand. Earth. Planet. Sci. Lett. 484, 92–102.
Hua, J., Fischer, K.M., Wu, M., Blom, M.,N.A., 2020. New approaches to multifrequency Sp stacking tested in the Anatolian region. J. Geophys. Res. https://doi.org/10.1029/2020JB020313.
Jackson, I., Faul, U.H., 2010. Grainsize-sensitive viscoelastic relaxation in olivine: towards a robust laboratory-based model for seismological application. Phys. Earth Planet. Int. 183, 151–163.
Jackson, I., Faul, U.H., Fitz Gerald, J.D., Morris, S.J.S., 2006. Contrasting viscoelastic behavior of melt-free and melt-bearing olivine: implications for the nature of grain-boundary sliding. Mater. Sci. Eng. 442, 170–174. https://doi.org/10.1016/J.Msea.2006.01.136.
James, E.K., Dalton, C.A., Gaherty, J.B., 2014. Rayleigh wave phase velocities in the Atlantic upper mantle. Geochem. Geophys. Geosyst. 15, 4305–4324. https://doi.org/10.1002/2014GC005518.
Jordan, T.H., 1978. Composition and development of the continental tectosphere. Nature 274, 544–548.
Jordan, T.H., Paulson, E.M., 2013. Convergence depths of tectonic regions from an ensemble of global tomographic models. J. Geophys. Res. 118, 4196–4225. https://doi.org/10.1002/jgrb.50263.
Karato, S.I., 2012. On the origin of the asthenosphere. Earth. Planet. Sci. Lett. 321, 95–103.
Karato, S.I., Jung, H., 1998. Water, partial melting and the origin of the seismic low velocity and high attenuation zone in the upper mantle. Earth. Planet. Sci. Lett. 157, 193–207.
Karato, S.-I., Park, J., 2019. On the origin of the upper mantle seismic discontinuities. In: Yuan, H., Romanowicz, B.A. (Eds.), Lithospheric Discontinuities, 239. AGU Geophysical Monograph, pp. 5–34. https://doi.org/10.1002/9781119249740.ch8.
Karato, S.I., Olugboji, T., Park, J., 2015. Mechanisms and geologic significance of the mid-lithosphere discontinuity in the continents. Nat. Geol. 8, 509–514.
Katz, R.F., Spiegelman, M., Langmuir, C.H., 2003. A new parameterization of hydrous mantle melting (2003, Sep 9). Geochem. Geophys. Geosys. 4 (9), 1073. https://doi.org/10.1029/2002gc000433.
Kawakatsu, H., Kumar, P., Takei, Y., Shinohara, M., Kanazawa, T., Araki, E., Suyehiro, K., 2009. Seismic evidence for sharp lithosphere-asthenosphere boundaries of oceanic plates. Science 324, 499–502.
Kennett, B.L.N., 2015. Lithosphere–asthenosphere P-wave reflectivity across Australia. Earth. Planet. Sci. Lett. 431, 225–235.
Kennett, B.L., Engdahl, E.R., Buland, R., 1995. Constraints on seismic velocities in the Earth from traveltimes. Geophys. J. Int. 122, 108–124.
Kennett, B.L.N., Yoshizawa, K., Furumura, T., 2017. Interactions of multi-scale heterogeneity in the lithosphere: Australia. Tectonophysics 717, 193–213.
Kind, R., Mooney, E., Yuan, X., 2020. New insights into the structural elements of the upper mantle beneath the contiguous United States from S-to-P converted seismic waves. Geophys. J. Int. 222, 646–659.
Kind, R., Yuan, X., 2019. Perspectives of the S-receiver-function-method to image lithospheric discontinuities. In: Yuan, H., Romanowicz, B.A. (Eds.), Lithospheric Discontinuities, 239. AGU Geophysical Monograph, pp. 139–154. https://doi.org/10.1002/9781119249740.ch8.
Kind, R., Yuan, X., Kumar, P., 2012. Seismic receiver functions and the lithosphere–asthenosphere boundary. Tectonophysics 536–537, 25–43.
Kind, R., Sodoudi, F., Yuan, X., Shomali, H., Roberts, R., Gee, D., Eken, T., Bianchi, M., Tilmann, F., Balling, N., Jacobsen, B.H., Kumar, P., Geissler, W.H., 2013. Scandinavia: a former Tibet. Geochem. Geophys. Geosyst. 14, 4479–4487. https://doi.org/10.1002/ggge.20251.
Kind, R., Handy, M.R., Yuan, X., Meier, T., Kampf, H., Soomro, R., 2017. Detection of a new sub-lithospheric discontinuity in Central Europe with S-receiver functions. Tectonophysics 700–701, 19–31. https://doi.org/10.1016/j.tecto.2017.02.002.
Knapmeyer-Endrun, B., Kruger, F., Geissler, W.H., PASSEQ Working Group, 2017. Upper mantle structure across the Trans-European Suture Zone imaged by S-receiver functions. Earth Planet Sci. Lett. 458, 429–441.
Korenaga, T., Korenaga, J., 2008. Subsidence of normal oceanic lithosphere, apparent thermal expansivity, and seafloor flattening. Earth Planet. Sci. Lett. 268, 41–51. https://doi.org/10.1016/J.Epsl.2007.12.022.
Kumar, P., Kawakatsu, H., 2011. Imaging the seismic lithosphere-asthenosphere boundary of the oceanic plate. Geochem. Geophys. Geosyst. 12.
Kumar, P., Yuan, X., Kumar, M.R., Kind, R., Li, X., Chadha, R.K., 2007. The rapid drift of the Indian tectonic plate. Nature 449, 894–897. https://doi.org/10.1038/nature06214.
Kumar, P., Kind, R., Yuan, X., Mechie, J., 2012. USArray receiver function images of the lithosphere–asthenosphere boundary. Seism. Res. Lett. 83, 486–491.
Kustowski, B., Ekstrom, G., Dziewonski, A.M., 2008. Anisotropic shear-wave velocity structure of the Earth's mantle: a global model. J. Geophys. Res. 113, 1–23.
Laske, G., Masters, G., Ma, Z., Pasyanos, M., 2013. Update on CRUST1.0 - a 1-degree global model of Earth's crust. In: EGU Gen. Assem. 2013, 15, p. 2658.
Lebedev, S., van der Hilst, R.D., 2008. Global upper-mantle tomography with the automated multimode inversion of surface and S-wave forms. Geophys. J. Int. 173, 505–518.
Lebedev, S., Boonen, J., Trampert, J., 2009. Seismic structure of Precambrian lithosphere: new constraints from broad-band surface wave dispersion. Lithos 109, 96–111. https://doi.org/10.1016/j.lithos.2008.06.010.
Lee, C.-T.A., 2006. Geochemical/petrologic constraints on the origin of cratonic mantle. In: Benn, K., Mareschal, J.-C., Condie, K.C. (Eds.), Archean Geodynamics and Environments, 164. AGU Geophysical Monograph, pp. 89–114.
Lee, C.-T.A., Luffi, P., Chin, E.J., 2011. Building and destroying continental mantle. Ann. Rev. Earth Planet. Sci. 39, 59–90. https://doi.org/10.1146/annurev-earth-040610-133505.
Lekic, V., Fischer, K.M., 2014. Contrasting lithospheric signatures across the western United States revealed by Sp receiver functions. Earth. Planet. Sci. Lett. 402, 90–98. https://doi.org/10.1016/j.epsl.2013.11.026.
Lekic, V., Romanowicz, B., 2011. Inferring upper-mantle structure by full waveform tomography with the spectral element method. Geophys. J. Int. 185, 799–831.
Lekic, V., French, S.W., Fischer, K.M., 2011. Lithospheric thinning beneath rifted regions of Southern California. Science 334, 783–787. https://doi.org/10.1126/science.1208898.
Levander, A., Miller, M.S., 2012. Evolutionary aspects of lithosphere discontinuity structure in the western U.S. Geochem. Geophys. Geosyst. 13, Q0AK07 https://doi.org/10.1029/2012GC004056.
Levin, V., Park, J., 1997. P-SH conversions in a flat-layered medium with anisotropy of arbitrary orientation. Geophys. J. Int. 131, 253–266.
Ligorria, J.P., Ammon, C.J., 1999. Iterative deconvolution and receiver-function estimation. Bull. Seism. Soc. Am. 89, 1395–1400.
Lin, P., Gaherty, J.B., Jin, G., Collins, J., Lizarralde, D., Evans, R.L., Hirth, G., 2016. High-resolution seismic constraints on flow dynamics in the ocean asthenosphere. Nature 535, 538–541. https://doi.org/10.1038/nature18012.
Liu, L., Morgan, J.P., Xu, Y., Menzies, M., 2018. Craton destruction 1: Cratonic keel delamination along a weak midlithospheric discontinuity layer. J. Geophys. Res. 123, 10–040.
Ma, Z., Dalton, C.A., 2019. Evidence for dehydration-modulated small-scale convection in the oceanic upper mantle from seafloor bathymetry and Rayleigh wave phase velocity. Earth. Planet. Sci. Lett. 510 https://doi.org/10.1016/j.epsl.2018.12.030.
Ma, Z., Dalton, C.A., Russell, J.B., Gaherty, J.B., Hirth, G., Forsyth, D.W., 2020. Shear attenuation and anelastic mechanisms in the central Pacific upper mantle. Earth. Planet. Sci. Lett. 536, 116148.
Maggi, A., Debayle, E., Priestley, K., Barruol, G., 2006. Multimode surface waveform tomography of the Pacific Ocean: a closer look at the lithospheric cooling signature. Geophys. J. Int. 166, 1384–1397. https://doi.org/10.1111/j.1365-246x.2006.03037.x.
Mancinelli, N.J., Fischer, K.M., Dalton, C.A., 2017. How sharp is the cratonic lithosphere-asthenosphere transition? Geophys. Res. Lett. 44, 10–189.
Mareschal, J.C., Jaupart, C., 2004. Variations of surface heat flow and lithospheric thermal structure beneath the North American craton. Earth Planet. Sci. Lett. 223, 65–77.
Masters, G., Barmine, M.P., Kientz, S., 2007. Mineos user's manual. In: Computational Infrastructure for Geodynamics. California Institute of Technology.
Mehouachi, F., Singh, S., 2018. Water-rich sublithospheric melt channel in the equatorial Atlantic Ocean. Nat. Geosci. 11 https://doi.org/10.1038/s41561-017-0034-z, 65-69.
Miller, M.S., Eaton, D.W., 2010. Formation of cratonic mantle keels by arc accretion: evidence from S receiver functions. Geophys. Res. Lett. 37, 1–5. https://doi.org/10.1029/2010GL044366.
Miller, M.S., O'Driscoll, L.J., Butcher, A.J., Thomas, C., 2015. Imaging Canary Island hotspot material beneath the lithosphere of Morocco and southern Spain. Earth Planet. Sci. Lett. 431, 186–194.
Montagner, J.P., 2002. Upper mantle low anisotropy channels below the Pacific Plate. Earth Planet. Sci. Lett. 202, 263–274.
Morgan, J.P., Parmentier, E.M., Lin, J., 1987. Mechanisms for the origin of midocean ridge axial topography - implications for the thermal and mechanical structure of

accreting plate boundaries. J. Geophys. Res. 92, 12823–12836. https://doi.org/10.1029/JB092iB12p12823.
Nettles, M., Dziewonski, A., 2008. Radially anisotropic shear velocity structure of the upper mantle globally and beneath North America. J. Geophys. Res. 113, B2. https://doi.org/10.1029/2006JB004819.
Nishimura, C.E., Forsyth, D.W., 1989. The anisotropic structure of the Upper Mantle in the Pacific. Geophys. J. I. 96, 203–229.
O'Driscoll, L.J., Miller, M.S., 2015. Lithospheric discontinuity structure in Alaska, thickness variations determined by Sp receiver functions. Tectonics 34, 694–714.
Ohira, A., Kodaira, S., Nakamura, Y., Fujie, G., Arai, R., Miura, S., 2017. Evidence for frozen melts in the mid-lithosphere detected from active-source seismic data. Scientific Reports 7, 15770.
Olugboji, T.M., Karato, S.I., Park, J., 2013. Structures of the oceanic lithosphere-asthenosphere boundary: mineral-physics modeling and seismological signatures. Geochem. Geophys. Geosyst. 14, 880–901.
Olugboji, T.M., Park, J., Karato, S.I., Shinohara, M., 2016. Nature of the seismic lithosphere-asthenosphere boundary within normal oceanic mantle from high-resolution receiver functions. Geochem. Geophys. Geosyst. 17, 1265–1282.
Panning, M.P., Lekic, V., Romanowicz, B.A., 2010. Importance of crustal corrections in the development of a new global model of radial anisotropy. J. Geophys. Res. 115, B12325.
Parsons, B., Sclater, J.G., 1977. Analysis of variation of ocean-floor bathymetry and heat-flow with age. J. Geophys. Res. 82, 803–827.
Pearson, D.G., Carlson, R.W., Shirey, S.B., Boyd, F.R., Nixon, P.H., 1995. Stabilization of Archean lithospheric mantle: a Re-Os isotope study of peridotite xenoliths from the Kaapvaal craton. Earth Planet Sci. Lett. 134, 341–357.
Pedersen, H.A., Fishwick, S., Snyder, D.B., 2009. A comparison of cratonic roots through consistent analysis of seismic surface waves. Lithos 109, 81–95. https://doi.org/10.1016/j.lithos.2008.09.016.
Perry, H.K.C., Forte, A.M., Eaton, D.W.S., 2003. Upper-mantle thermochemical structure belowNorth America from seismic-geodynamic flow models. Geophys. J. Int. 154, 279–299.
Plank, T., Forsyth, D.W., 2016. Thermal structure and melting conditions in the mantle beneath the Basin and Range province from seismology and petrology. Geochem. Geophys. Geosyst. 17 https://doi.org/10.1002/2015GC006205.
Pollack, H.N., Hurter, S.J., Johnson, J.R., 1993. Heat flow from the Earth's interior: analysis of the global data set. Rev. Geophys. 31, 267–280.
Pollitz, F.F., Mooney, W.D., 2016. Seismic velocity structure of the crust and shallow mantle of the Central and Eastern United States by seismic surface wave imaging. Geophys. Res. Lett. 43, 118–126.
Porritt, R.W., Allen, R.M., Pollitz, F.F., 2014. Seismic imaging east of the Rocky Mountains with USArray. Earth Planet. Sci. Lett. 402, 16–25. https://doi.org/10.1016/j.epsl.2013.10.034.
Porritt, R.W., Miller, M.S., Darbyshire, F.A., 2015. Lithospheric architecture beneath Hudson Bay. Geochem. Geophys. Geosys. 16, 2262–2275.
Porter, R., Zandt, G., McQuarrie, N., 2011. Pervasive lower-crustal seismic anisotropy in Southern California: evidence for underplated schists and active tectonics. Lithosphere 3, 201–220.
Priestley, K., McKenzie, D., 2006. The thermal structure of the lithosphere from shear wave velocities. Earth Planet. Sci. Lett. 244, 285–301. https://doi.org/10.1016/J.Epsl.2006.01.008.
Priestley, K., McKenzie, D., 2013. The relationship between shear wave velocity, temperature, attenuation and viscosity in the shallow part of the mantle. Earth Planet. Sci. Lett. 381, 78–91.
Rader, E., Emry, E., Schmerr, N., Frost, D., Cheng, C., Menard, J., Yu, C.Q., Geist, D., 2015. Characterization and petrological constraints of the midlithospheric discontinuity. Geochem. Geophys. Geosys. 16, 3484–3504.
Reeves, Z., Lekić, V., Schmerr, N., Kohler, M., Weeraratne, D., 2015. Lithospheric structure across the California Continental Borderland from receiver functions. Geochem. Geophys. Geosys. 16, 246–266.
Revenaugh, J., Jordan, T.H., 1991. Mantle layering from ScS reverberations: 3. The upper mantle. J. Geophys. Res. 96, 19781–19810.
Richardson, S.H., Gurney, J.J., Erlank, A.J., Harris, J.W., 1984. Origin of diamonds in old enriched mantle. Nature 310, 198–202.
Richter, F.M., 1973. Convection and large-scale circulation of mantle. J. Geophys. Res. 78, 8735–8745.
Ritsema, J., Deuss, A., van Heijst, H.J., Woodhouse, J.H., 2011. S40RTS: A degree-40 shear velocity model for the mantle from new Rayleigh wave dispersion, teleseismic traveltime and normal-mode splitting function measurements. Geophys. J. Int. 184, 1223–1236.
Ritsema, J., van Heijst, H.J., Woodhouse, J.H., 2004. Global transition zone tomography. J. Geophys. Res. 109(B2).
Ritzwoller, M.H., Shapiro, N.M., Zhong, S.J., 2004. Cooling history of the Pacific lithosphere. Earth Planet. Sci. Lett. 226, 69–84. https://doi.org/10.1016/J.Epsl.2004.07.032.
Rudnick, R.L., Nyblade, A.A., 1999. The thickness and heat production of Archean lithosphere: constraints from xenolith thermobarometry and surface heat flow. In: Fei, Y., Bertka, C.M., Mysen, B.O. (Eds.), Mantle Petrology: Field Observations and High Pressure Experimentation: A Tribute to Francis R. (Joe) Boyd. The Geochemical Society, St. Louis, MO, pp. 3–12.
Russell, J.B., Gaherty, J.B., Lin, P.Y.P., Lizarralde, D., Collins, J.A., Hirth, G., Evans, R.L., 2019. High-resolution constraints on Pacific upper mantle petrofabric inferred from surface-wave anisotropy. J. Geophys. Res. 124, 631–657. https://doi.org/10.1029/2018JB016598.
Rychert, C.A., Harmon, N., 2017. Constraints on the anisotropic contributions to velocity discontinuities at ~60 km depth beneath the Pacific. Geochem. Geophys. Geosys. 18, 2855–2871.
Rychert, C.A., Harmon, N., 2018. Predictions and observations for the oceanic lithosphere from S-to-P receiver functions and SS precursors. Geophys. Res. Lett. 45, 5398–5406. https://doi.org/10.1029/2018gl077675.
Rychert, C.A., Harmon, N., Constable, S., Wang, S., 2020. The Nature of the Lithosphere-Asthenosphere Boundary. J. Geophys. Res. https://doi.org/10.1029/2018JB016463.
Rychert, C.A., Shearer, P.M., 2009. A global view of the lithosphere-asthenosphere boundary. Science 324, 495–498. https://doi.org/10.1126/science.1169754.
Rychert, C.A., Shearer, P.M., 2011. Imaging the lithosphere-asthenosphere boundary beneath the Pacific using SS waveform modeling. J. Geophys Res. 116.
Rychert, C.A., Fischer, K.M., Rondenay, S., 2005. A sharp lithosphere-asthenosphere boundary imaged beneath eastern North America. Nature 436, 542–545. https://doi.org/10.1038/nature03904.
Rychert, C.A., Shearer, P.M., Fischer, K.M., 2010. Scattered wave imaging of the lithosphere-asthenosphere boundary. Lithos 120, 173–185. https://doi.org/10.1016/j.lithos.2009.12.006.
Rychert, C.A., Hammond, J.O., Harmon, N., Kendall, J.M., Keir, D., Ebinger, C., Bastow, I.D., Ayele, A., Belachew, M., Stuart, G., 2012. Volcanism in the Afar Rift sustained by decompression melting with minimal plume influence. Nature Geo. 5, 406–409. https://doi.org/10.1038/NGEO1455.
Rychert, C.A., Harmon, N., Tharimena, S., 2018a. Seismic imaging of the base of the ocean plates. In: Yuan, H., Romanowicz, B.A. (Eds.), Lithospheric Discontinuities, 239. AGU Geophysical Monograph, pp. 71–87. https://doi.org/10.1002/9781119249740.ch8.
Rychert, C.A., Harmon, N., Tharimena, S., 2018b. Scattered wave imaging of the oceanic plate in Cascadia. Sci. Adv. 4, eaao1908 https://doi.org/10.1126/sciadv.aao1908.
Rychert, C.A., et al., 2019. A Dynamic Lithosphere-asthenosphere Boundary Dictated by Variations in Melt Generation and Migration: Results From the PI-LAB Experiment in the Equatorial Mid Atlantic, Abstract T41B-02, Presented at the AGU Fall Meeting, San Francisco, 9-13 Dec., 2019.
Saha, S., Dasgupta, R., Tsuno, K., 2018. High pressure phase relations of a depleted peridotite fluxed by CO_2-H_2O-bearing siliceous melts and the origin of mid-lithospheric discontinuity. Geochem. Geophys. Geosys. 19, 595–620.
Sakamaki, T., Suzuki, A., Ohtani, E., Terasaki, H., Urakawa, S., Katayama, Y., Funakoshi, K.I., Wang, Y., Hernlund, J.W., Ballmer, M.D., 2013. Ponded melt at the boundary between the lithosphere and asthenosphere. Nat. Geol. 6, 1041–1044. https://doi.org/10.1038/Ngeo1982.
Savage, B., Silver, P.G., 2008. Evidence for a compositional boundary within the lithospheric mantle beneath the Kalahari craton from S receiver functions. Earth Planet. Sci. Lett. 272, 600–609.
Schaeffer, A.J., Lebedev, S., 2013. Global shear speed structure of the upper mantle and transition zone. Geophys. J. Int. 194, 417–449.
Schaeffer, A.J., Lebedev, S., 2014. Imaging the North American continent using waveform inversion of global and USArray. Earth Planet. Sci. Lett. 402 https://doi.org/10.1016/j.epsl.2014.05.014.
Schaeffer, A.J., Lebedev, S., 2015. Global heterogeneity of the lithosphere and underlying mantle: a seismological appraisal based on multimode surface-wave dispersion analysis, shear-velocity tomography, and tectonic regionalization. In: The Earth's Heterogeneous Mantle. Springer International Publishing, pp. 3–46.
Schmandt, B., Lin, F.-C., Karlstrom, K.E., 2015. Distinct crustal isostasy trends east and west of the Rocky Mountain Front. Geophys. Res. Lett. 42 https://doi.org/10.1002/2015GL066593.
Schmerr, N., 2012. The Gutenberg Discontinuity: melt at the lithosphere-asthenosphere boundary. Science 335, 1480–1483.
Schulte-Pelkum, V., Mahan, K.H., 2014. A method for mapping crustal deformation and anisotropy with receiver functions and first results from USArray. Earth Planet. Sci. Lett. 402, 221–233.
Schutt, D.L., Lesher, C.E., 2006. Effects of melt depletion on the density and seismic velocity of garnet and spinel lherzolite. J. Geophys. Res. 111, B05401 https://doi.org/10.1029/2003JB002950.
Selway, K., Yuan, H., Romanowicz, B.A., 2019. Electrical discontinuities in the continental lithosphere imaged with magnetotellurics. In: Lithospheric Discontinuities, 239. AGU Geophysical Monograph, pp. 89–110. https://doi.org/10.1002/9781119249740.ch8.
Selway, K., Ford, H., Kelemen, P., 2015. The seismic mid-lithosphere discontinuity. Earth Planet. Sci. Lett. 414, 45–57.
Shapiro, N.M., Ritzwoller, M.H., 2002. Monte-Carlo inversion for a global shear-velocity model of the crust and upper mantle. Geophys. J. Int. 151, 88–105.
Shapiro, S.S., Hager, B.H., Jordan, T.H., 1999. The continental tectosphere and Earth's long-wavelength gravity field. Lithos 48, 135–152.
Shearer, P.M., Buehler, J., 2019. Imaging upper-mantle structure under USArray using long-period reflection seismology. J. Geophys. Res. 124, 9638–9652.
Shen, W., Ritzwoller, M.H., 2016. Crustal and uppermost mantle structure beneath the United States. J. Geophys. Res. 121, 4306–4342. https://doi.org/10.1002/2016JB012887.
Shito, A., Suetsugu, D., Furumura, T., Sugioka, H., Ito, A., 2013. Small-scale heterogeneities in the oceanic lithosphere inferred from guided waves. Geophys. Res. Lett. 40, 1708–1712.
Shito, A., Suetsugu, D., Furumura, T., 2015. Evolution of the oceanic lithosphere inferred from Po/So waves traveling in the Philippine Sea Plate (2015, Jul). J. Geophys. Res. 120 (7), 5238–5248. https://doi.org/10.1002/2014jb011814.
Sim, S.J., Spiegelman, M., Stegman, D.R., Wilson, C., 2020. The influence of spreading rate and permeability on melt focusing beneath mid-ocean ridges. Phys. Earth Planet. Int. 106486.

Simmons, N.A., Forte, A.M., Boschi, L., Grand, S.P., 2010. GyPSuM: a joint tomographic model of mantle density and seismic wave speeds. J. Geophys. Res. 115, B12310 https://doi.org/10.1029/2010JB007631.
Sleep, N.H., 2005. Evolution of the continental lithosphere. Annu. Rev. Earth Planet. Sci. 33, 369–393.
Snyder, D.B., Humphreys, E., Pearson, D.G., 2017. Construction and destruction of some North American cratons. Tectonophysics 694, 464–485.
Sodoudi, F., Yuan, X., Kind, R., Lebedev, S., Adam, J.M.C., Kastle, E., Tilmann, F., 2013. Seismic evidence for stratification in composition and anisotropic fabric within the thick lithosphere of Kalahari Craton. Geochem. Geophys. Geosys. 14, 5393–5412. https://doi.org/10.1002/2013GC004955.
Sparks, D., Parmentier, E., 1991. Melt extraction from the mantle beneath spreading centers. Earth and Planetary Science Letters 105 (4), 368–377.
Stein, C.A., Stein, S., 1992. A model for the global variation in oceanic depth and heat-flow with lithospheric age. Nature 359, 123–129.
Steinberger, B., Becker, T.W., 2018. A comparison of lithospheric thickness models. Tectonophysics 746, 325–338. https://doi.org/10.1016/j.tecto.2016.08.001.
Stern, T.A., Henrys, S.A., Okaya, D., Louie, J.N., Savage, M.K., Lamb, S., Sato, H., Sutherland, R., Iwasaki, T., 2015. A seismic reflection image for the base of a tectonic plate. Nature 518, 85–88. https://doi.org/10.1038/nature14146.
Stixrude, L., Lithgow-Bertelloni, C., 2011. Thermodynamics of mantle minerals – II. Phase equilibria. Geophys. J. Int. 184, 1180–1213. https://doi.org/10.1111/j.1365-246X.2010.04890.x.
Sun, W., Kennett, B.L.N., 2017. Mid-lithosphere discontinuities beneath the western and central North China Craton. Geophys. Res. Lett. 44, 1302–1310. https://doi.org/10.1002/2016GL071840.
Sun, D., Miller, M.S., Piana Agostinetti, N., Asimow, P.D., Li, D., 2014. High frequency seismic waves and slab structures beneath Italy. Earth Planet. Sci. Lett. 391, 212–223.
Takei, Y., Holtzman, B.K., 2009. Viscous constitutive relations of solid-liquid composites in terms of grain boundary contiguity: 1. Grain boundary diffusion control model. J. Geophys. Res. 114.
Takeo, A., Nishida, K., Isse, T., Kawakatsu, H., Shiobara, H., Sugioka, H., Kanazawa, T., 2013. Radially anisotropic structure beneath the Shikoku Basin from broadband surface wave analysis of ocean bottom seismometer records. J. Geophys. Res. 118, 2878–2892. https://doi.org/10.1002/jgrb.50219.
Tan, Y., Helmberger, D.V., 2007. Trans-Pacific upper mantle shear velocity structure. J. Geophys. Res. 112.
Tharimena, S., Rychert, C., Harmon, N., White, P., 2017a. Imaging Pacific lithosphere seismic discontinuities—insights from SS precursor modeling. J. Geophys. Res. 122, 2131–2152.
Tharimena, S., Rychert, C., Harmon, N., 2017b. A unified continental thickness from seismology and diamonds suggests a melt-defined plate. Science 357, 580–583.
Thybo, H., Perchuc, E., 1997. The seismic 8° discontinuity and partial melting in the continental mantle. Science 275, 1626–1629.
Tonegawa, T., Helffrich, G., 2012. Basal reflector under the Philippine Sea plate. Geophys. J. Int. 189, 659–668.
Turcotte, D., Oxburgh, E.R., 1967. Finite amplitude convective cells and continental drift. J. Fluid Mech. 28, 29–42.
Wagner, L.S., Fischer, K.M., Hawman, R., Hopper, E., Howell, D., 2018. The relative roles of inheritance and long-term passive margin lithospheric evolution on the modern structure and tectonic activity in the southeastern United States. Geosphere 14, 1385–1410.
Watts, A., 1978. Analysis of isostacy in the worlds oceans. 1. Hawaiian-Emperor Seamount Chain. J. Geophys. Res. 83 (NB12), 5989–6004.
Wang, S., Constable, S., Rychert, C., Harmon, N., 2020. A lithosphere-asthenosphere boundary and partial melt estimated using marine magnetotelluric data at the central Middle Atlantic Ridge. https://doi.org/10.1029/2020GC009177.
Weeraratne, D.S., Forsyth, D.W., Fischer, K.M., Nyblade, A.A., 2003. Evidence for an upper mantle plume beneath the Tanzanian craton from Rayleigh wave tomography. J. Geophys. Res. 108, 2427. https://doi.org/10.1029/2002JB002273.
Wirth, E.A., Long, M.D., 2014. A contrast in anisotropy across mid-lithospheric discontinuities beneath the central United States—a relic of craton formation. Geology 42, 851–854.
Wittlinger, G., Farra, V., 2007. Converted waves reveal a thick and layered tectosphere beneath the Kalahari super-craton. Earth Planet. Sci. Lett. 254, 404–415. https://doi.org/10.1016/j.epsl.2006.11.048.
Wölbern, I., Rumpker, G., Link, K., Sodoudi, F., 2012. Melt infiltration of the lower lithosphere beneath the Tanzania craton and the Albertine rift inferred from S receiver functions. Geochem. Geophys. Geosys. 13, 1–20. https://doi.org/10.1029/2012GC004167.
Wu, F.Y., Yang, J.H., Xu, Y.G., Wilde, S.A., Walker, R.J., 2019. Destruction of the North China craton in the Mesozoic. Ann. Rev. Earth Planet. Sci. 47, 173–195.
Xu, P., Zhao, D., 2009. Upper-mantle velocity structure beneath the North China Craton: implications for lithospheric thinning. Geophys. J. Int. 177, 1279–1283. https://doi.org/10.1111/j.1365-246X.2009.04120.x.
Yamauchi, H., Takei, Y., 2016. Polycrystal anelasticity at near-solidus temperatures. J. Geophys. Res. 121, 7790–7820. https://doi.org/10.1002/2016jb013316.
Yuan, K., Beghein, C., 2013. Seismic anisotropy changes across upper mantle phase transitions. Earth. Planet. Sci. Lett. 374, 132–144.
Yuan, K., Beghein, C., 2014. Three-dimensional variations in Love and Rayleigh wave azimuthal anisotropy for the upper 800 km of the mantle. J. Geophys. Res. 119, 3232–3255.
Yuan, H., Levin, V., 2014. Stratified seismic anisotropy and the lithosphere-asthenosphere boundary beneath eastern North America. J. Geophys. Res. 119, 3096–3114.
Yuan, H., Romanowicz, B., 2010. Lithospheric layering in the North American craton. Nature 466, 1063–1069.
Yuan, X., Kind, R., Li, X., Wang, R., 2006. The S receiver functions: synthetics and data example. Geophys. J. Int. 165, 555–564.
Yuan, H., Romanowicz, B., Fischer, K.M., Abt, D., 2011. 3-D shear wave radially and azimuthally anisotropic velocity model of the North American upper mantle. Geophys. J. Int. 184, 1237–1260.